Archaeal lipid hydrogen isotopes in a marine thaumarchaeon

William Leavitt[1], Sebastian Kopf[2], Yuki Weber[3], Beverly Chiu[1], Jamie Mcfarlin[4], Felix Elling[5], Shelley Hoeft McCann[3], and Ann Pearson[6]

[1]Dartmouth College
[2]University of Colorado Boulder
[3]Harvard University
[4]University of Colorado
[5]Christian-Albrechts-Universität zu Kiel: Kiel, DE
[6]0000-0003-2785-8405

November 23, 2022

Abstract

The stable hydrogen isotope composition of persistent biomolecules is used as a paleoenvironmental proxy. While much previous work has focused on plant leaf wax-derived n-alkanes, the potential of bacterial and archaeal lipid biomarkers as carriers of H isotope signatures remains underexplored. Here we investigated H isotope distributions in the membrane lipids of the ammonia-oxidizing chemoautotroph Nitrosopumilus maritimus strain SCM1. Hydrogen isotope ratios were measured on the biphytane chains of tetraether membrane lipids extracted from steady-state continuous cultures cultivated at slow, medium, and fast growth rates. In contrast to recent work on bacterial fatty acids, where the direction and magnitude of isotopic fractionation varies widely (ca. 600 energy metabolism, archaeal biphytane data in the present work are relatively invariant. The weighted average 2H/1H fractionation values relative to growth water ($2\varepsilon L/W$) only ranged from 272 to 260 a three-fold difference in doubling times (30.8 hr to 92.5 hr), yielding an average growth-rate effect of 0.2 depleted than all heterotrophic archaeal and bacterial lipid H isotope measurements in the literature, and on par with those from other autotrophic archaea, as well as isoproenoid-based lipids in photoautotrophic algae. N. maritimus values of $2\varepsilon L/W$ also varied systematically with the number of internal rings (cyclopentyl + cyclohexyl), increasing for each additional ring by 6.4 ± 2.7 an isotope flux-balance model in tandem with a comprehensive analysis of the sources of H in archaeal lipid biosynthesis, we use this observation to estimate the kinetic isotope effects (KIEs) of H incorporation from water; from reducing cofactors such as ferredoxin, and for the transhydrogenation reaction(s) that convert the electron-donor derived NADH into NADPH for anabolic reactions. Consistent with prior studies on bacteria, our results indicate the KIEs of reducing cofactors and transhydrogenation processes in archaea are highly fractionating, while those involving exchange of water protons are less so. When combined with the observation of minimal growth-rate sensitivity, our results suggest biphytanes of autotrophic 3HP/4HB Thaumarchaeota may be offset from source waters by a nearly constant $2\varepsilon L/W$ value. Together with the ring effect, this implies that all biphytanes originating from a common source should have a predictable ordering of their isotope ratios with respect to biphytane ring number, allowing precise reconstruction of the original δ2H value of the growth water. Collectively, these patterns indicate archaeal biphytanes have potential as paleo-hydrological proxies, either as a complement or an alternative to leaf wax n-alkanes.

1
2
3   *Title:* Controls on the hydrogen isotope composition of tetraether lipids in a marine thaumarchaeon
4

5   *Authors*:
6   W. D. Leavitt[*,†,1,2], S. H. Kopf[3,†,*], Y. Weber[4,§], B. Chiu[1, ‡], J. M. McFarlin[3,4], F. J. Elling [5,6], S. Hoeft-
7   McCann[5,¥], A. Pearson[5,*]
8
9   [†]*Contributed equally*; **Correspondence;*
10
11   *Affiliations:*
12   1. Dartmouth Earth Sciences; 2. Dartmouth Chemistry; 3. Department of Geological Sciences, University of Colorado
13   Boulder, Boulder, Colorado 80309; 4. Department of Geology & Geophysics, University of Wyoming; 5. Department
14   of Earth & Planetary Sciences, Harvard University; 6. Leibniz-Laboratory for Radiometric Dating and Isotope
15   Research, Kiel University
16
17   *Current Address:*
18   [§]*Beam Theraputics;* [‡]*c16 biosciences;* [¥]Wellesley College.*

19
20   *Keywords*: Archaeal lipids, GDGTs, biphytanes, biomarkers
21
22

23 ## Abstract

24 The stable hydrogen isotope composition of persistent biomolecules is used as a
25 paleoenvironmental proxy. While much previous work has focused on plant leaf wax-derived *n*-
26 alkanes, the potential of bacterial and archaeal lipid biomarkers as carriers of H isotope signatures
27 remains underexplored. Here we investigated H isotope distributions in the membrane lipids of the
28 ammonia-oxidizing chemoautotroph *Nitrosopumilus maritimus* strain SCM1. Hydrogen isotope
29 ratios were measured on the biphytane chains of tetraether membrane lipids extracted from steady-
30 state continuous cultures cultivated at slow, medium, and fast growth rates. In contrast to recent
31 work on bacterial fatty acids, where the direction and magnitude of isotopic fractionation varies
32 widely (*ca.* 600 ‰ range) in response to the choice of substrate and pathways of energy
33 metabolism, archaeal biphytane data in the present work are relatively invariant. The weighted
34 average ^{2}H/^{1}H fractionation values relative to growth water ($^2\varepsilon_{L/W}$) only ranged from -272
35 to -260 ‰, despite a three-fold difference in doubling times (30.8 hr to 92.5 hr), yielding an
36 average growth-rate effect of 0.2 ‰ hr^{-1}. These $^2\varepsilon_{L/W}$ values are more depleted than all
37 heterotrophic archaeal and bacterial lipid H isotope measurements in the literature, and on par with
38 those from other autotrophic archaea, as well as isoproenoid-based lipids in photoautotrophic
39 algae. *N. maritimus* values of $^2\varepsilon_{L/W}$ also varied systematically with the number of internal rings
40 (cyclopentyl + cyclohexyl), increasing for each additional ring by 6.4 ± 2.7 ‰. Using an isotope
41 flux-balance model in tandem with a comprehensive analysis of the sources of H in archaeal lipid
42 biosynthesis, we use this observation to estimate the kinetic isotope effects (KIEs) of H
43 incorporation from water; from reducing cofactors such as ferredoxin, and for the
44 transhydrogenation reaction(s) that convert the electron-donor derived NADH into NADPH for
45 anabolic reactions. Consistent with prior studies on bacteria, our results indicate the KIEs of
46 reducing cofactors and transhydrogenation processes in archaea are highly fractionating, while
47 those involving exchange of water protons are less so. When combined with the observation of
48 minimal growth-rate sensitivity, our results suggest biphytanes of autotrophic 3HP/4HB
49 Thaumarchaeota may be offset from source waters by a nearly constant $^2\varepsilon_{L/W}$ value. Together with
50 the ring effect, this implies that all biphytanes originating from a common source should have a
51 predictable ordering of their isotope ratios with respect to biphytane ring number, allowing precise
52 reconstruction of the original δ^2H value of the growth water. Collectively, these patterns indicate
53 archaeal biphytanes have potential as paleo-hydrological proxies, either as a complement or an
54 alternative to leaf wax *n*-alkanes.
55

1. Introduction

The relative abundances of protium (^{1}H) and deuterium (^{2}H) in water track a wide variety of physical, hydrological, and climate parameters (Gat, 1996; Hayes, 2001; Robert, 2001). Certain biomolecules incorporate these isotopes at predictable ratios (δ^2H values) relative to their source water, preserving a record of conditions at the time of synthesis. Indeed some lipid hydrogen isotope compositions can survive in the sedimentary record for millions of years, encoding past changes in Earth system processes, from tectonics to hydroclimate to local ecology (Sessions et al., 2004; Schimmelmann et al., 2006; Sessions, 2016). The H isotopic ratios of biomolecules utilized for reconstructing past environments and ecologies have been studied broadly in photoautotrophic organisms, as well as in a variety of chemoautotrophic and heterotrophic bacteria (e.g., (Sessions et al., 1999; Zhang et al., 2009; Dawson et al., 2015; Sachs and Kawka, 2015; Maloney et al., 2016; Osburn et al., 2016; Sachs et al., 2016, 2017; Wolfshorndl et al., 2019)). To date, however, there are few reports for the archaea (Kaneko et al., 2011; Dirghangi and Pagani, 2013; Wu et al., 2020; Lengger et al., 2021). In part this taxonomic bias originates from the long history of experimental and field study on leaf plant waxes and marine phytoplankton (Estep and Hoering, 1980; Sessions et al., 1999; Sachse et al., 2012; Sachs, 2014), but it also arises from a lack of systematic understanding of how archaeal biomarkers are biosynthesized (Jain et al., 2014; Pearson, 2019; Zeng et al., 2019), how archaeal lipid δ^2H values reflect growth waters, as well as analytical challenges in the H isotope analysis of archaeal ether lipids (Lengger *et al.*, 2021). Unlocking the historical archive of archaeal lipid H isotopes requires examining the biochemical controls on their lipid-water isotope effects ($^2\varepsilon_{L/W}$).

The expression of $^2\varepsilon_{L/W}$ in geostable lipids reflects not only incorporation of environmental water, but also the kinetic isotope effects (KIEs) of enzymes involved in energy conservation, central metabolism, and the pathway(s) of lipid biosynthesis. In plants and eukaryotic algae the $^2\varepsilon_{L/W}$ between growth water and long-chain *n*-alkanes (plant waxes) captures changes in hydroclimate, as many of the biosynthetic and metabolic KIEs are similar between these taxa (Smith and Freeman, 2006; Hou et al., 2008; Sachse et al., 2010, 2012; Kahmen et al., 2011; McInerney et al., 2011), although a quarter of the observed variance could also be due to genetic factors (Bender et al., 2016). Experimental calibration of lipid $^2\varepsilon_{L/W}$ from eukaryotic microalgae therefore focuses on constraining the response to physical parameters such as temperature, salinity, and irradiance (Sachs, 2014; Sachs and Kawka, 2015; van der Meer et al., 2015; Maloney et al., 2016; Sachs et al., 2016, 2017; Wolfshorndl et al., 2019). In contrast to eukaryotic examples, bacterial lipids show considerably more complexity. Multiple taxa have been studied with respect to their $^2\varepsilon_{L/W}$ offsets from growth water, as well as for differences between metabolism-specific processes and use of different substrates (Sessions et al., 1999, 2002; Valentine et al., 2004; Campbell et al., 2009; Zhang et al., 2009; Dawson et al., 2015; Heinzelmann et al., 2015b; Osburn et al., 2016; Leavitt et al., 2016; Campbell et al., 2017; Leavitt et al., 2017; Heinzelmann et al., 2018; Wijker et al., 2019). Such work shows that $^2\varepsilon_{L/W}$ can be exceptionally large in bacteria, varying by several *percent* in

95   both the positive and negative directions. Broad patterns of $^2\varepsilon_{L/W}$ values distinguish bacterial
96   chemoautotrophs (-400‰ to -200‰), oxygen producing photoautotrophs (-250‰ to -150‰), and
97   aerobic and anaerobic heterotrophs (-150‰ to +300‰) (Sessions et al., 2002; Valentine et al.,
98   2004; Kreuzer-Martin et al., 2006; Campbell et al., 2009, 2017; Zhang et al., 2009; Dawson et al.,
99   2015; Heinzelmann et al., 2015; Osburn et al., 2016; Leavitt et al., 2016; Leavitt et al., 2016;
100 Leavitt et al., 2017; Wijker et al., 2019).

101

102 Archaea generate some of the most diagenetically robust and structurally diagnostic lipids, yet
103 have been little studied, with currently only a few reports of axenic culture natural abundance lipid
104 δ^2H and enriched isotope studies. The natural abundance lipid δ^2H studies were conducted with a
105 mesophilic halophile (Dirghangi and Pagani, 2013), a thermoacidophile and a single marine
106 sediment sample (Kaneko et al., 2011), and a thermoacidophile and two natural samples (Lengger
107 et al., 2021). The axenic deuterium isotope enrichment study used a methanogen (Wu et al., 2020),
108 as well as a suite of mixed culture studies focused on anaerobic methane oxidizers (Kellermann et
109 al., 2016; Wegener et al., 2016). The archaeal biomarkers most critical to paleoenvironmental
110 reconstructions are the glycerol dibiphytanyl glycerol tetraethers (iGDGTs), compounds that are
111 found as a series of structural homologs containing from zero to eight cyclopentane rings (most
112 commonly $\leq$ 6; iGDGT-0, -1, … -6); or in the case of crenarchaeol, a lipid believed to be unique
113 to Thaumarchaeota, one cyclohexane and four cyclopentane rings (Oger and Cario, 2013; Pearson
114 and Ingalls, 2013; Schouten et al., 2013; Elling et al., 2017). The primary application of iGDGT
115 biomarkers to date has been marine paleothermometry (Schouten et al., 2002), which requires
116 calibration of iGDGT ring distributions to growth temperature and other environmental forcing,
117 both in the laboratory and in modern core-top samples (e.g., (Kim et al., 2008, 2010; Tierney and
118 Tingley, 2014, 2015; Hurley et al., 2016; Elling et al., 2017; Cobban et al., 2020; Dunkley Jones
119 et al., 2020; Zhou et al., 2020). The ring distributions of thermoacidophiles provide important
120 context to this work by investigating the interaction between temperature changes and other growth
121 determinants such as pH, energy availability, and redox status (Boyd et al., 2011, 2013; Feyhl-
122 Buska et al., 2016; Quehenberger et al., 2020; Zhou et al., 2020; Tourte et al., 2022). Similarly
123 detailed work is needed to understand the $^2\varepsilon_{L/W}$ isotope signatures of GDGTs so we may evaluate
124 their potential as hydrologic cycle proxies.

125

126 In this study we determined the H isotope fractionation between iGDGTs and growth water for the
127 ammonia-oxidizing archaeal (AOA) chemoautotroph *Nitrosopumilus maritimus* SCM1
128 (Thaumarchaeota), Strain SCM1 was cultivated continuously under chemically static (chemostat)
129 conditions at a range of cellular doubling times. The growth and metabolic rates were controlled
130 by increasing or decreasing the energy flux (terminal electron acceptor donor delivery rate) of the
131 supply medium; for prior examples of this approach with archaea, see (Hurley et al., 2016;
132 Quehenberger et al., 2020; Zhou et al., 2020). For all trials, we quantified the magnitude of $^2\varepsilon_{L/W}$
133 for the full set of biphytane (BP) hydrocarbons liberated by ether cleavage from acid extractable
134 total iGDGTs. We present values from BP-0, BP-1, BP-2, and BP-3. The results indicate that $^2\varepsilon_{L/W}$

135 for *N. maritimus* remains nearly constant between fast, medium, and slow growth rates. The results
136 suggest that the ubiquitous iGDGTs of mesophilic autotrophs have potential as paleo-hydrological
137 proxies. The hydrogen isotope ratios of mesophilic archaeal iGDGTs and their derivative BPs may
138 be reliably and consistently offset from local growth waters.
139
140

2. Methods

2.1 Culture conditions

143 Continuous (chemostat) cultures of *N. maritimus* SCM1 were grown on modified Synthetic
144 Crenarchaeota Medium with 1 mM NH_4Cl as previously described (Martens-Habbena et al., 2009;
145 Hurley et al., 2016), but with the following modifications: 300 µM α-ketoglutaric acid was added
146 as a H_2O_2 scavenger (Kim et al., 2016; Bayer et al., 2019), and a balance-controller loop was used
147 to maintain a constant dilution rate (my-Control™, Applikon, Delft, the Netherlands). In the 1.6 L
148 reactor temperature was held constant at 28 ℃, and the pH of the initial medium was adjusted to
149 7.8, which yielded in-situ pH of 7.52 to 7.56 over the course of the experiments at steady state.
150 Nitrite concentrations and pH values for *N. maritimus* remained stable within analytical precision
151 (nitrite ±0.03 mM; pH ±0.01). The *N. maritimus* experiments were run in a single bioreactor and
152 maintained steady state conditions throughout the sampling intervals. The dilution rate was set to
153 yield cell doubling times (T_D) of 30.8, 46.2, and 92.5 h. Upon reaching steady state, the outflow
154 of each bioreactor was collected continuously into a chilled vessel (0 to 4 °C) for between 1 and 4
155 days. *N. maritimus* cells were isolated by filtration onto combusted 0.3 µm GF-75 glass fiber filters
156 (Sterlitech, Kent, WA, USA). Filters were stored at -80 or -20 °C until processing for lipid
157 analysis.
158

2.2 Lipid extraction and biphytane preparation

160 Core iGDGTs were extracted from freeze-dried pellets and filters by acid hydrolysis followed by
161 ultrasonic solvent extraction as described previously (Zhou et al., 2020). Briefly, samples were
162 incubated in 3 N methanolic HCl (33% water content) for 90 min at 65°C. Methyl tert-butyl ether
163 (MTBE) was added at a ratio of 3:2 (acid:MTBE, v:v), and samples were sonicated for 5 min
164 (Qsonica Q500, Newtown, CT, USA). After sonication, *n*-hexane was added at a ratio of 1:1
165 (MTBE:hexane, v:v), vortexed, and centrifuged (3 min, 15,000 *g*). The organic upper layer was
166 collected, dried under N_2, and separated into two fractions over activated Al_2O_3 by elution with
167 dichloromethane (DCM; non-polar lipids), and DCM:methanol (1:1, v:v; iGDGTs). Ether bonds
168 were cleaved in 57 % HI (4h at 120°), and the resulting alkyl iodides were reduced to alkanes
169 (BPs) with H_2 in the presence of $Pt^{(IV)}O_2$ (Kaneko et al., 2011). Before analysis, BPs were purified
170 over activated Al_2O_3 by elution with *n*-hexane. Samples of *N. maritimus* were collected in large
171 volumes and reflect single extracts.
172

173   **2.3 Hydrogen isotope analyses and data reduction**

174   Biphytane $^2H/^1H$ ratios were analyzed by gas chromatography pyrolysis isotope ratio mass
175   spectrometry (GC-P-IRMS) on a GC IsoLink II IRMS System (Thermo Scientific), consisting of
176   a Trace 1310 GC fitted with a programmable temperature vaporization (PTV) injector and either
177   a 30 m ZB5HT column (i.d. = 0.25 mm, 0.25 μm, Phenomenex, Torrance, CA, USA) or a 60 m
178   DB1 column (i.d. = 0.25 mm, 0.25 μm, Agilent, Santa Clara, CA, USA), ConFlo IV interface, and
179   253 Plus mass spectrometer (Thermo Scientific). Sample runs using the ZB5HT column used a
180   fast ramp of the PTV to 400°C for sample transfer to the GC column and initial hold of the column
181   at 60°C for 2 min, the GC oven was ramped to 350°C over the course of 14.5 min at a rate of 20°C
182   /min, followed by an isothermal hold at 350°C for 7 minutes during which all biphytanes eluted
183   (see Figure S1). Sample runs using the DB1 column used a fast ramp of the PTV to 330°C for
184   sample transfer to the GC column and initial hold of the column at 60°C for 2 min, the GC oven
185   was ramped to 220°C over the course of 7 min at a rate of 22°C /min, then to 330°C over the course
186   of 14 min at a rate of 8°C /min, followed by an isothermal hold at 330°C for 20 minutes during
187   which all biphytanes eluted.

188

189   All $^2H/^1H$ ratios are reported in delta notation (δ^2H) in permil (‰) units relative to the international
190   seawater standard on the VSMOW-SLAP (Vienna Standard Mean Ocean Water, Standard Light
191   Antarctic Precipitation) scale. All $^2H/^1H$ fractionation factors are reported in epsilon notation ($^2\varepsilon$)
192   in permil (‰). All peak amplitudes are reported in volts (V) and refer to the amplitude of the *m/z*
193   2 measurement which has an operational amplifier with a 10^9 Ω resistor and thus reflects nA
194   currents. Values of δ^2H were first determined relative to H_2 reference gas (δ^2H_{raw}), and then
195   calibrated externally using a standard *n*-alkane mixture (A6, containing C_{15} through C_{30} *n*-alkanes
196   spanning from -9 to -263 ‰ vs. VSMOW; A. Schimmelmann, Indiana University). The A6
197   standard was combined with a C_{36} *n*-alkane (nC_{36}, -259.2 ‰ vs. VSMOW; A. Schimmelmann,
198   Indiana University) and measured at regular intervals at different concentrations. The BP hydrogen
199   isotope calibration was performed in R based on 2195 compound-specific measurements from the
200   A6 standard with peak amplitudes from 0.80 to 36 V (*m/z* 2) using the packages *isoreader* (v 1.3.0,
201   (Kopf et al., 2021) and *isoprocessor* (v 0.6.11) available at github.com/isoverse. To correct for
202   offset, scale compression and the peak-size effect inherent in δ^2H measurements (Liu et al., 2022),
203   the following multivariate linear regression was inverted and applied to all standards and samples
204   to determine δ^2H_{cal}:

205

206    $$\delta^2 H_{raw} = \beta_0 + \beta_1 \cdot \delta^2 H_{cal} + \beta_2 \cdot A + \beta_3 \cdot \delta^2 H_{cal} \cdot \sqrt{A} \qquad \text{(Eq. 1)}$$

207

208   where *A* signifies peak amplitude (*m/z* 2), and δ^2H_{cal} is the actual H-isotope composition of the
209   analytes (known values for standard compounds; calibrated values for target compounds after
210   inversion). The overall RMSE of calibration was 4.9‰ and residuals showed a random distribution
211   (Figure S2, Panel 4), whereas other simpler regression models had substantially larger errors and
212   showed systematic trends in their residuals (for a comparison of several different regression

213   models see Figure S2). To assess the uncertainty introduced by sample matrix and low signal-to-
214   noise ratios, each biphytane peak was integrated multiple times in the Isodat software (v 3.0,
215   Thermo Scientific), with manual background correction set before and after the eluting analyte
216   peak. This analysis suggested integration errors to be negligible. Finally, to accurately assess peak-
217   size dependent analytical uncertainty, the n-C_{36} standard was analyzed throughout in combination
218   with the A6 standard because of its similar retention time to the biphytanes (elutes between BP-0
219   and BP-1). It was purposefully excluded from the calibration (Eq. 1) and was instead used to
220   estimate the analytical error of the biphytane H isotope measurements after calibration using a
221   local polynomial regression fit across all 73 n-C_{36} measurements spanning peak amplitudes from
222   0.06 to 27 V (m/z 2). This provided realistic peak-size adjusted error estimates of the calibrated
223   measurements (σ_{cal}) with steep increases in the observed error at low peak amplitudes stepping
224   from 3.9‰ at analyte peak amplitudes of 5V to 14‰ at 2V and 34‰ at 1V (Figure S3).

225

226   Calibrated δ^2H values for the biphytanes were corrected for the H added during hydrogenation of
227   alkyl iodides. Assuming a similar isotope effect associated with the PtO_2-catalzyed reaction of H_2
228   and alkyl iodides as previously reported ($^2\varepsilon_{hydrog}$ = -721 ± 177 ‰; (Kaneko et al., 2011)), and the
229   measured δ^2H value of the H_2 tank (δ^2H_{H2} = -64 ± 2 ‰; courtesy of Andrew Masterson,
230   Northwestern University, IL, USA), the final corrected δ^2H values were calculated using the
231   following equation:

232

233    $$\delta^2H_{cor} = \left(1 + \frac{2}{n_H}\right) \cdot \delta^2H_{cal} - \frac{2}{n_H} \cdot \left(\left(\,^2\varepsilon_{hydrog} + 1\right) \cdot (\delta^2H_{H2} + 1) - 1\right) \qquad \text{(Eq. 2)}$$

234

235   where n_H is the number of original H atoms in each alkyl chain. The total analytical uncertainty of
236   the corrected δ^2H values was calculated using standard error propagation (Eq. 3) of the peak-size
237   adjusted error estimates and hydrogenation correction assuming all errors to be uncorrelated. The
238   hydrogenation correction ranged from 10.3 to 12.7 ‰ and increased analytical uncertainty by up
239   to 1.9 ‰.

240

241    $$\sigma_{cor} = \sqrt{\left(\frac{\partial(\delta^2H_{cor})}{\partial(\delta^2H_{cal})} \cdot \sigma_{cal}\right)^2 + \left(\frac{\partial(\delta^2H_{cor})}{\partial(\delta^2H_{H2})} \cdot \sigma_{H2}\right)^2 + \left(\frac{\partial(\delta^2H_{cor})}{\partial(\,^2\varepsilon_{hydrog})} \cdot \sigma_{hydrog}\right)^2} \qquad \text{(Eq. 3)}$$

242

243   Hydrogen isotope analysis of growth medium water (δ^2H_{water}) was conducted with filter-sterilized
244   media samples collected at the time of biomass sampling using an H-device (pyrolysis to H_2 gas)
245   coupled to a dual-inlet IRMS (Thermo Delta Plus XL) and measured relative to a calibrated
246   reference tank at 0.5‰ measurement uncertainty (1σ) (Taenzer et al., 2020). The resulting values
247   of δ^2H were calibrated to the water isotope equivalent using standards of known composition. The
248   hydrogen isotope fractionation between growth water and BP lipids ($^2\varepsilon_{L/W}$) was calculated
249   according to Eq. 4:

250

251 $$^2\varepsilon_{L/W} = \left[\frac{(^2\delta_{cor}+1000)}{(^2\delta_{water}+1000)} - 1\right] \cdot 1000 \qquad\qquad\qquad (Eq.\ 4)$$

252

253 Corrected bipythane δ^2H_{cor} values (Figure S1) and resulting $^2\varepsilon_{L/W}$ fractionation factors from sample
254 and analytical replicates (n $\geq$ 4 in all cases) were averaged for each experimental condition and are
255 reported in Table 1 and visualized in Figure 1 (individual measurement values are in Table S1;
256 Figure S1A). All averages are weighted means of individual measurements ($1/\sigma^2$ weights) to
257 account for the amplitude-dependent range in uncertainties. The reported error estimate of each
258 average is the larger of the standard deviation of all replicates vs. the propagated uncertainty from
259 individual measurements. Changes in $^2\varepsilon_{L/W}$ per ring ($\Delta\varepsilon$/ring) were calculated as the average of
260 isotope ratios for all combinations of $(\delta BP(x) - \delta BP(y < x))/$(ring difference x-y) (Table 1).

261

2.4 Model Implementation

263 An isotope mass balance model to interpret the resulting $^2\varepsilon_{L/W}$ values was solved by implementing
264 a simulated annealing routine (*simulannealbnd*) of the Matlab Global Optimization Toolbox
265 (Matlab V2021b), using Monte Carlo resampling approaches (10^4 runs per trial). This approach
266 minimizes the error cost function for multivariable optimization problems within prescribed
267 bounds. It is agnostic to the presence of multiple local minima and is applicable to non-linear
268 functions.

269

270

3. Results

272 Consistent with prior reports of the iGDGT distributions in *N. maritimus* SCM1 (Hurley et al.,
273 2016; Elling et al., 2017), the relative abundances of BPs averaged 0.22:0.29:0.29:0.20 for BP-0,
274 -1, -2, and -3, respectively (Figure S1C, Table 1), where BP-3 represents the cyclohexane-
275 containing moiety of crenarchaeol. More details of the parent iGDGT compositions that yield these
276 BP distributions, as well as the lipid responses to cultivation at steady state in chemostats, are
277 available elsewhere (Hurley et al., 2016; Zhou et al., 2020).

278

279 The BPs were depleted in ^2H relative to growth water by as little as 257 ‰ (BP-3) to as much as
280 279 ‰ (BP-0) (Figure 1; Table 1). The abundance-weighted mean $^2\varepsilon_{L/W}$ value across all biphytanes
281 from *N. maritimus* was -266 ± 9 ‰ (based on $n = 73$ total data points; Table 1, Table S1, Figure
282 S1A). All growth conditions exhibit a systematic, ring-dependent change in the isotopic
283 composition of their biphytanes (Figure 1; also see probability density distributions for each BP in
284 Figure S1A) with decreasing $^2\varepsilon_{L/W}$ (enriched in ^2H) as the number of cyclic moieties increases.
285 Though small, this effect appears to be real, as there is no systematic correlation between δ^2H
286 residuals (*i.e.*, measurement accuracy) and peak intensities (Figure S1A) and changes in precision

287 are accounted for based on an internal standard (n-C_{36}) that has similar chromatographic retention
288 to the biphytanes (Figure S3 and details in the Methods section). BPs -1, -2, and -3 were on average
289 5.3, 15, and 18 ‰ enriched in ^2H relative to the acyclic BP-0. Overall, each additional ring
290 contributes a 6.4 ± 2.7 ‰ increase to biphytane δ^2H values across the full dataset. This pattern
291 appears only minimally affected by differences in growth rate, with a positive, growth rate-
292 dependent linear trend that is statistically insignificant (Figure 1).
293
294

4. Isotope flux-balance model

296 To generalize these findings and pave the way for future work with other archaea, we constructed
297 an isotope flux-balance model (Figure 2) to explain both the magnitude of and patterns within the
298 observed $^2\varepsilon_{L/W}$ values for *N. maritimus* (Figure 1). This analysis provides insight into the
299 biochemical origins of archaeal $^2\varepsilon_{L/W}$ patterns and highlights their potential for proxy applications.
300
301 *N. maritimus* SCM1 grows autotrophically by the 3-hydroxypropionate/4-hydroxybutyrate
302 (3HP/4HB) cycle using NH_4^+ as the electron donor (Könneke et al., 2014). It was chosen to explore
303 potential impacts of growth rate variability on $^2\varepsilon_{L/W}$ patterns expressed by 3HP/4HB archaea, given
304 the goal of developing an environmental proxy based on BPs of the globally ubiquitous, ammonia
305 oxidizing Thaumarchaeota. Therefore, some sections of our isotope model and the ensuing
306 discussion may not be applicable to all archaea; below we aim to distinguish between universal
307 vs. metabolism-specific information.
308

4.1. Sources of hydrogen in archaeal lipid synthesis

310 In chemo(litho)autotrophic archaea, the hydrogen in lipid biosynthesis derives directly from
311 intracellular water, from metabolic cofactors such as **NADPH**, or from inorganic cofactors such
312 as ferredoxin (**Fd**; where the hydride (H^-) is abstracted from H_2O) (Figures 2 and 3; Figure S4 and
313 S5). In heterotrophs there is also the potential for incorporation from organic substrate (e.g.,
314 glucose). NADPH is primarily derived from NADH via the electron transport chain. Minor
315 additional amounts of NADPH may also be obtained from central metabolism (e.g., from
316 isocitrate), but here we assume this source can be folded into the total NADPH pool. Given this
317 complexity, we first examined in detail the origin of H in all biosynthetic steps to biphytanes and
318 calculated stoichiometric scenarios – dependent on different source options – to serve as a
319 framework for isotopic interpretations.
320

4.1.1 Synthesis of archaeal isoprenoids

322 In archaea, the synthesis of BP hydrocarbons proceeds as follows. Isopentenyl pyrophosphate
323 (IPP) is synthesized from three units of acetyl CoA (Ac-CoA) using the mevalonate pathway
324 (Figure 3, steps 1-6; (Chen et al., 1994; Koga and Morii, 2007; Hayakawa et al., 2018). Three units

325 of IPP and one of its isomer DMAPP together condense to yield geranylgeranyl diphosphate
326 (GGPP, not shown; (Chen and Poulter, 1993)). The hydrogen in IPP derives both from the original
327 acetate and from HMG-CoA reductase using NADPH as co-factor, while isomerization between
328 IPP and DMAPP (Figure 3, step 6) also incorporates one H from water in place of one originally
329 contributed by acetate. If the formation of DMAPP is limited to the minimum required to initiate
330 isoprenoid condensation (1:3, DMAPP:IPP), only a single terminal H in the resulting GGPP retains
331 the water signature. Additional water H (f_w) can be introduced either during IPP/DMAPP
332 interconversion (Figure 3, step 6), and/or potentially during tautomerization of acetoacetyl-CoA
333 (Figure 3, step 2), where if IPP-DMAPP isomerase is rapid relative to steps 7 and 8, then more
334 water-derived H may be carried into the isoprenoid product. Thus, there is a range of stoichiometry
335 possible for the fractional contribution of water-derived H, the consequences of which are
336 elaborated below. Condensation of two di-O-geranylgeranyl glycerol phosphate (DGGGP) units
337 into the membrane-spanning tetraether by the Tes enzyme eliminates two H, which would be of
338 mixed water and acetate origin (Figure 3, step 8) (Zeng et al., 2022). Ring formation is catalyzed
339 by GrsA and GrsB (Zeng et al., 2019) (Figure 3, step 9) and does not add any net hydrogen, but
340 likely replaces some acetate-derived H with water-derived H. Saturation (Figure 3, step 10) is
341 catalyzed by geranylgeranyl reductase (GGR). The electron donor for GGR in *N. maritimus* is not
342 yet known, so for simplicity, we merge all electron-donor options into two choices: NADPH
343 (Figure 3, step 10a) – i.e., we give GGR the signature of the NADPH pool used in steps 1-8; *or,*
344 biosynthetic H is divided between NADPH and alternative oxidoreductases, namely those based
345 on iron-sulfur clusters, e.g., ferredoxin (Fd), which we hypothesize could be the specific donor for
346 GGR (Figure 3, step 10b).
347
348 Combining these ideas – high versus low extent of water exchange, and two potential types of
349 hydride donors for GGR – yields four generalized permutations for archaeal isoprenoid
350 biosynthesis, henceforth called Scenarios 1-4 (Table 2, Table S1).
351
352 **4.1.2. Stoichiometric accounting: H sources in archaeal biphytanes**
353 The four scenarios yield different budgets for the stoichiometry of biphytane H sources. Most of
354 the 80 H atoms in the C_{40} alkyl chain of the acyclic biphytane (BP-0) are inherited from methyl-H
355 of Ac-CoA (f_A, fractional contribution from Ac-CoA). Hydrides (H$^-$) are introduced from NADPH
356 during biosynthesis of the mevalonate precursor to IPP ($f_{LipSynth\_NADPH}$), as well as during the final
357 saturation of the alkyl chains by GGR in the scenarios where NADPH is the H-donor (f_{GGR_NADPH});
358 in both cases the paired protons (H$^+$) are obtained from water ($f_{LipSynth\_W}$, f_{GGR_W}). Alternatively, if
359 Fd serves as the reductant to GGR, both H ultimately source from water (Isobe et al., 2014), but
360 with potentially different isotope effects for the hydride and the proton. We therefore include a
361 separate pool of H$^-$ from Fd (f_{GGR_Fd}), while combining the paired H$^+$ with the water pool. Finally,
362 for Scenarios 3 and 4, in which water is assumed to exchange freely with acetoacetyl-CoA during
363 synthesis of IPP and DMAPP and IPP may rapidly isomerize, the model contains an exchangeable
364 water fraction (f_x). The resulting stoichiometry of H sources to BP-0 is summarized in Table 2,

365   Table S1, and Figure S5. This accounting model is widely applicable across the archaea, i.e., it is
366   not specific to the 3HP/4HB-pathway, and later can be utilized for other autotrophs, as well as
367   heterotrophs (Figure 2B).
368

4.1.3. Sources of H in Ac-CoA generated autotrophically by the 3HP/4HB cycle

370   For any archaeon that grows as an autotroph, all three H of the Ac-CoA methyl group also derive
371   originally from water. These H can be conceptualized as (*i*) direct incorporation of cellular water,
372   or (*ii*) donation from reducing cofactors. The 3HP/4HB cycle generates Ac-CoA with a predicted
373   ratio of 2:1 for direct water and cofactor hydrogens using reasonable biochemical assumptions for
374   the mechanism of each step (see Figure S4). Thus, when there is no direct incorporation of H from
375   organic substrates, the H assigned to Ac-CoA can be apportioned 0.67:0.33 among the water and
376   NADPH pools of lipid biosynthesis (LipSynth). For example, re-distributing the 47 ⅓ H of Ac-
377   CoA in Scenario 1 yields the following cumulative fractions: $f_{LipSynth\_W}$ = 0.83% +
378   (0.6667)*59.17% = 40.28% and $f_{LipSynth\_NADPH}$ = 20% + (0.3333)*59.17% = 39.72%; see Table S1
379   for all proportions.
380

4.1.4. Summary budget and the impact of ring number

382   The stoichiometric budget for biphytane H sources in *N. maritimus* was further simplified for
383   isotope flux balance analysis: water-derived H from lipid biosynthesis ($f_{LipSynth\_W}$) was combined
384   with GGR water protons (f_{GGR_W}) to yield total direct water H (f_{*W}), and NADPH-derived hydrides
385   from lipid biosynthesis ($f_{LipSynth\_NADPH}$) were combined with hydrides associated with GGR
386   (f_{GGR_NADPH}) to yield total NADPH sources (f_{*NADPH}).
387

388   $$BP = \left(f_{LipSynth_W} + f_{GGR_W}\right) + \left(f_{LipSynth_{NADPH}} + f_{GGR_{NADPH}}\right) + f_{GGR_{Fd}} + f_x$$
389   $$= f_{*W} + f_{*NADPH} + f_{Fd} + f_x \qquad\qquad (Eq.\ 5)$$
390

391   Ring additions can be described by a formula that accounts for the proportional change in each H
392   source (Eq. 6).
393

394   $$f_i^r = (f_i^0 + \Delta H_i \cdot r/n)/(1 - 2 \cdot r/n) \qquad\qquad (Eq.\ 6)$$
395

396   Here, the fractional contribution f_i^r of each H source i changes with the number of pentacyclic
397   rings (r); f_i^0 is the fractional contribution of each source to BP-0; n is the number of H in BP-0
398   (= 80); and ΔH_i is the change in the number of hydrogens for each fraction per additional ring.
399   The denominator reflects that for each additional pentacyclic ring, the molecule has 2 fewer H
400   overall. The stoichiometry of adding a ring is not as straightforward as eliminating the
401   incorporation of one H⁻ from GGR or Fd and one H⁺ from water, where some substitution also is
402   expected due to the mechanism of the ring cyclization reaction by radical *S*-adenosylmethionine
403   proteins (Zeng et al., 2019), where one 1 H per ring is replaced (Pearson, 2019). For each f_i^r, the
404   corresponding values of ΔH_i in *N. maritimus* are then as follows:

405
406   With NADPH as reductant:
407   For f_{GGR_NADPH}, $\Delta H_{GGR\_NADPH} = -1 \,/\, ring$
408   For f_{GGR_W}, $\Delta H_{GGR\_W} = -\,^2/_3 \,/\, ring$
409   For $f_{LipSynth\_NADPH}$, $\Delta H_{LipSynth\_NADPH} = -\,^1/_3 \,/\, ring$
410
411   With Fd as reductant:
412   For f_{GGR_Fd}, $\Delta H_{GGR\_Fd} = -1 \,/\, ring$
413   For f_{GGR_W}, $\Delta H_{GGR\_W} = -\,^2/_3 \,/\, ring$
414   For $f_{LipSynth\_NADPH}$, $\Delta H_{LipSynth\_NADPH} = -\,^1/_3 \,/\, ring$
415

416   The full stoichiometry of BP isomers -0, -1, -2, and -3 across Scenarios 1-4 is summarized in Table
417   S1, which is calculated by combining Eq. 6 with Eq. 5 (*see* example in Figure S5). In all cases,
418   having more rings is equivalent to having fractionally more water-derived H (Table 3). For
419   scenarios in which Fd is modeled to be the electron donor to GGR, more rings also are somewhat
420   counterintuitively associated with more H from NADPH (e.g., nearly 2% more for BP-3 in
421   Scenario 2; Table 3), but these extra reducing equivalents are offset by having less H from Fd-
422   hydride.
423

4.2. Hydrogen isotope flux balance model for archaeal biphytanes

425   Our quantitative model follows established approaches (e.g., Wijker et al., 2019). It divides the H
426   isotope flux balance into two modules (Figure 2):
427
428   (1) *Cellular production* of NADH from the exogenous electron donor with H transfer to
429   NADPH (transhydrogenation).
430   (2) *Biphytane synthesis* from water and the NADPH pool, plus the option to use Fd as an
431   additional electron donor for GGR as explained in Section 4.1. For *N. maritimus* these
432   are the only major sources of biphytane-H. For future analysis of heterotrophic archaea,
433   this module also allows for incorporation of H directly from assimilated, rather than
434   catabolized, organic substrates (not used for *N. maritimus*).
435

436   The H fluxes for *Biphytane synthesis* are set using the biosynthetic sources (Eq. 5). Solving the
437   associated isotope budget for biphytane synthesis requires an estimate of the $^2H/^1H$ ratio of the
438   NADPH pool, which is used throughout the cell and can have a variable isotope ratio depending
439   on supply:demand, i.e., growth efficiency (Wijker et al., 2019). This necessitates the separate
440   *Cellular production* module in which the pool of NADPH can vary. In ammonia-oxidizing
441   (autotrophic) archaea, the only presumed source of NADPH is through an (as-yet unidentified)
442   transhydrogenation reaction with NADH (Figure 2A) generated by the electron transport chain
443   during ammonia oxidation (Walker et al., 2010). In heterotrophs, the sources of NADPH, and

444   therefore the potential effects on ^{2}H/^{1}H ratios of the NADPH pool, are more complex due to
445   additional catabolic fluxes from organic precursors (Zhang et al., 2009; Wijker et al., 2019), which
446   can also differ substantially between archaea and bacteria (Bräsen et al., 2014).
447

448   **4.2.1. Cellular production module – Determining flux and isotope balance for NADPH**
449   To allow for growth-rate dependent effects, this module permits reducing power (f_E, exogenous
450   electron source) to be recycled as a leakage flux, f_L (Eq. 7). In a slight modification of the approach
451   of Wijker et al. (2019), we symbolize this not as excess NADPH production, but rather an excess
452   of electrons cycling through the NADH↔NAD$^+$ pool. Thus f_N, the production of NADPH co-
453   factors from transhydrogenation of NADH, has a high fractional demand on f_E when the NADH
454   supply (ammonia oxidation rate) is slow.

455

456   Mass balance, "*Cell*" module: $f_E \equiv 1 = f_N + f_L$ (Eq. 7)

457

458   The unused reducing power, or leakage, is modeled as a function of the energy available to the cell
459   according to a parameterization factor λ. Both a slow growth rate (high T_D) and a low value of λ
460   (highly efficient cell) decrease f_L. The cell is thus growing with maximum efficiency ($f_L \rightarrow 0$) at
461   the slowest, most energy-starved doubling time (T_{D_max}; where $X_{TD} = 1$) (Eq. 8, 9).

462

463   Unused reducing power: $f_L = \lambda(1 - X_{TD})$ (Eq. 8)

464   Growth rate dependence of f_L: $X_{Td} = \dfrac{T_D - T_{D\text{-min}}}{T_{D\text{-max}} - T_{D\text{-min}}}$; $\; f_L \downarrow$ as $T_D \uparrow$ and/or $\lambda \downarrow$ (Eq. 9)

465
466   Combining these equations yields the isotope balance for NADPH production in ammonium
467   oxidizing archaea, where all f_i are fractional fluxes and all R_i are ^{2}H/^{1}H ratios (Eq. 10, 11). Here,
468   the ^{2}H/^{1}H ratio of NADPH is controlled by the fractionation relative to the electron donor pool
469   (α_E, presumed to yield incoming NADH offset from R_W), in combination with the fractionation
470   associated with the unknown transhydrogenation process (α_{TH}). The magnitude of R_{NADPH} is thus
471   offset from R_{NADH} by a constant ($R_{NADPH} = \alpha_{TH}R_{NADH}$) and R_{NADH} varies as a function of f_N; see
472   Figure S6. Note that these equations for cellular production of NAPDH are not universal and would
473   require metabolism-specific modifications if used for other autotrophs or heterotrophs, whereas
474   the biphytane synthesis module is generalizable.

475   Isotope balance, "*Cellular production*" module: $R_{NADH} = \alpha_E R_W / (\alpha_{TH} + \lambda(1 - X_{TD})(1 - \alpha_{TH}))$
476   (Eq. 10)

477   Then substitute (see Figure S6):

$$R_{NADPH} = \alpha_{TH} R_{NADH}$$
$$= \alpha_{TH} \alpha_E R_W / (\alpha_{TH} + \lambda(1 - X_{TD})(1 - \alpha_{TH}))$$

Eq. 11)

478

479   **4.2.2. Biphytane synthesis module – Determining flux and isotope balance for BPs**

480   The value of R_{NADPH} (Eq. 11) is needed to calculate R_{BP} in the *Biphytane synthesis* module (Figure
481   2B, lower half). We presume all water protons are governed by a common KIE (α_W) and that all
482   NADPH hydride sources have a single isotope effect α_{NADPH}. The alternate source of GGR
483   reductants is symbolized by ferredoxin (f_{Fd}), with a potentially different isotope effect, α_{Fd}. To
484   allow for isomerization-related exchange of water protons, we include the variable f_x ("exchange")
485   with isotope effect α_x. The direct substrate flux, γ, would transmit unfractionated H directly from
486   substrate to BPs; it is included to accommodate future modeling of heterotrophic taxa. The mass
487   balance for biphytane synthesis is given by combining Eq. 5 with the γ term, which then yields the
488   full isotope balance:

489

490   Isotope balance, "*Biphytane synthesis*" module:

491   $$R_{BP} = (1 - \gamma)[(f_{*W}\alpha_W + f_x\alpha_x + f_{Fd}\alpha_{Fd})R_W + f_{*NADPH}\alpha_{NADPH}R_{NADPH}] + \gamma R_S$$

(Eq. 12)

492

493   Substitute Eq. 11 to obtain the isotope ratios of BPs:

494

495   $$R_{BP} = (1 - \gamma)\left[f_{*W}\alpha_W + f_x\alpha_x + f_{Fd}\alpha_{Fd} + \frac{f_{*NADPH}\alpha_{NADPH}\alpha_E\alpha_{TH}}{\alpha_{TH} + L(1 - X_{TD})(1 - \alpha_{TH})}\right]R_W + \gamma R_S$$

(Eq. 13)

496

497   While Eq. 13 may describe the values and patterns for the $^2H/^1H$ ratios of biphytanes, it contains
498   eight unknowns: γ, λ, and all six isotope effects, α_i. The problem is reducible, however, through
499   a combination of supported assumptions, and by having data for multiple biphytanes, each at
500   several different growth rates. These controlled variants impart predictable changes to the
501   stoichiometric fractions, f_i, yet the corresponding values of R_{BP} must be satisfied using a single set
502   of KIEs, α_i, unique to the organism. Additionally, the model must account for the observation that
503   cyclopentane rings increase the $^2H/^1H$ ratio by > 6 ‰ ring^{-1} in response to shifts among the
504   fractional hydrogen sources (Table 3). Cyclopentane rings are formed as an alternative to
505   saturation by GGR, and therefore it may be informative to view the pattern from the opposite
506   perspective: every GGR-mediated reduction (H$^-$ + H$^+$) decreases $^2\varepsilon_{L/W}$ by -6.4 ‰ for a ~ 2/80
507   increase in total H budget. Thus, the net process of electron donation must have a negative KIE:

508 roughly -260‰ (= -6.4 ‰ ÷ 2/80) averaged across both the hydride and the proton. This is
509 consistent with the overall $^2\varepsilon_{L/W}$ expressed for these organisms. It further indicates that the KIE
510 associated with hydride donation is large, given prior assertions that the KIE of water incorporation
511 is relatively small (Zhang et al., 2009; Wijker et al., 2019). Thus, we implemented a Monte-Carlo
512 resampling approach to estimate all values of α_i and examine the results in the context of these
513 data patterns. The respective scenarios and solutions are outlined below.
514
515 **4.2.3. Model solutions, N. maritimus – Scenario 1: NADPH, no ferredoxin**
516 In *N. maritimus*, γ is zero, reducing the problem to seven unknowns. Data for the four BPs and
517 three growth conditions (T_{D-min} and T_{D-max} assumed to be 20 h and 120 hr; (Könneke et al., 2005;
518 Santoro and Casciotti, 2011)) were modeled as follows.
519
520 Scenario 1: $f_x = 0$, $f_{Fd} = 0$; i.e., no extra water exchange and NADPH is the only H⁻ source.
521         $\lambda < 0.5$ electron donor flux is up to 50% leaky
522         $\alpha_W > 0.5$; $\alpha_W = 0.9$ water isotope effects may be moderate or small
523         $\alpha_{TH} = 0.01\text{-}1.0$ electron donor isotope effects may be large
524         $\alpha_E \cdot \alpha_{NADPH} = 0.669$ see Scenario 2 for details
525
526 While setting $f_{Fd} = 0$ can reproduce the relative patterning of $^2\varepsilon_{L/W}$ values for BPs of different ring
527 numbers, i.e., BP-0 < … < BP-3, no implementation of this scenario can produce a large enough
528 difference to match the data. Scenario 1 yields a maximum +3.1 ‰ ring⁻¹ at the limit of $\alpha_{TH} = 0.01$,
529 and this value yields too large a growth-rate effect (>> 0.2 ‰ hr⁻¹) due to the interdependence of
530 α_{TH} and λ (Eq. 13). Conversely, at the correct growth-rate effect, the per-ring difference is no
531 larger than +1.2 ‰ ring⁻¹. All attempts to adjust individual parameters failed to fix this deficiency,
532 indicating Scenario 1 is oversimplified.
533
534 **4.2.4. Model solutions, N. maritimus – Scenario 2: ferredoxin as reductant for GGR**
535 If *N. maritimus* uses Fd as the H⁻ source for GGR, this not only alters the stoichiometric proportions
536 of f_{*W}, f_{*NADPH}, and f_{Fd} for biosynthesis (Table 2), it also affects the proportional changes in these
537 flux ratios at variable BP ring numbers (Table 3). This scenario can fully mimic the data and
538 therefore was explored more completely.
539
540 Scenario 2: $f_x = 0$; Fd supplies H⁻ for GGR; NADPH supplies remaining lipid H⁻.
541   Re-sampling range, initial conditions:
542         $\lambda < 1$ full range of leakiness permitted
543         $\alpha_W = 0.9$ constant (Zhang et al., 2009; Wijker et al., 2019)
544   α_{TH} and $\alpha_{Fd} = 0.01\text{-}1.0$ electron donor isotope effects may be large
545         $\alpha_E \cdot \alpha_{NADPH} = 0.01\text{-}1.0$ Case A, wide range
546         $\alpha_{NADPH} = 0.9$, $\Rightarrow \alpha_E = \alpha_E \cdot \alpha_{NADPH} \cdot 0.9^{-1}$ Case B, assumed $\alpha_{NADPH} = \alpha_W$

547

548   The value of α_W was constrained before solving for the other values of α_i. We initially set α_W to

549   float between 0.5-1.0, under the assumption that this value would be both moderate and variable.

550   However, all model runs consistently yielded a value of $\alpha_W \geq 0.9$ for the allowed solution space.

551   Based on this outcome and its agreement with prior literature (Zhang et al., 2009; Wijker et al.,

552   2019), we then fixed $\alpha_W = 0.9$, both here and retroactively in Scenario 1. Moderate changes in the

553   value assigned to α_W affect the absolute values of the model outcomes but do not affect the relative

554   patterns. Based on this apparently small isotope effect for α_W, we also chose to bypass any

555   scenarios that allowed isomerization-related exchange with water (f_x); i.e., we permanently set f_x

556   = 0 and eliminated Scenarios 3 and 4, as they seem inconsistent with the strong ^{2}H-depletion

557   indicated by the data.

558

559   <u>Case A</u>: The values of α_E and α_{NADPH} cannot be determined independently because their product

560   occurs in the numerator of a single term (Eq. 13). Acknowledging this, we first ran the model with

561   a wide allowed range (0.01-1.0) for the hydride transfer reactions α_{TH} and α_{Fd} and for the product,

562   $\alpha_E \cdot \alpha_{NADPH}$. This approach narrowly defined the optimal value of $\alpha_E \cdot \alpha_{NADPH}$ (0.669, $R^2 > 0.99$;

563   Table 4, Figure S6B) regardless of the values of the other parameters. <u>Case B</u>: As an alternative,

564   we defined $\alpha_{NADPH} = \alpha_W$. This is the implicit approach taken by Wijker et al. (2019) for the case

565   of bacterial fatty acids assuming NADPH hydrides are transferred to fatty acids directly (i.e.,

566   without explicit α_{NADPH}), but with the acknowledgement that this H may undergo water exchange.

567   When we adopt this alternative approach, α_E becomes uniquely 0.743 in the best-fit solution, given

568   that $\alpha_E \cdot \alpha_{NADPH}$ must remain 0.669 (Table 4).

569

570   Regardless of how the components of $\alpha_E \cdot \alpha_{NADPH}$ are defined, only a narrow range of solutions is

571   possible for α_{Fd}. The mean best-fit values are 0.14 ± 0.02 and 0.132 (with error < model bin step),

572   respectively, for the two cases. This is equivalent to ε_{Fd} = -860 to -868‰ (Figure 4A, Table 4),

573   which is as or more fractionating than current estimates for membrane-bound transhydrogenases

574   ($^2\varepsilon_{PntAB}$, -758 ‰; Jackson et al., 1999; Wijker et al., 2019).

575

576   In contrast, the solution for α_E (0.743) – or more robustly, the solution for the product $\alpha_E \cdot \alpha_{NADPH}$

577   (0.669) – is less fractionating than the estimate for α_{Fd} or bacterial PntAB. The process symbolized

578   by α_E, however, is not transhydrogenation, but rather the net KIE for transfer of H from the

579   inorganic electron donor by the electron transport chain, in which a membrane-bound electron

580   harvesting respiratory complex 1 (e.g., NDH1 a.k.a. Nuo (Walker et al., 2010)) is the likely source

581   of NADH production (Figure 2A). To our knowledge, specific characterization of the hydrogen

582   KIE for NDH1 has not been done; however, as NADH is the initial source of all reducing hydrides

583   in *N. maritimus*, we expect that the solution for α_E must be < α_W to yield strong ^{2}H-depletion in

584   lipids, and as a result also in net biomass.

585

586　The remaining unknowns are λ and α_{TH}, and again there is no unique solution (Eq. 13; Figure
587　S6C). However, every optimized combination of λ and α_{TH} must not only reproduce the ring-
588　dependence of the isotope composition of the individual BPs, but it must also show the observed
589　sensitivity (slope, ‰ hr^{-1}) of $^2\varepsilon_{L/W}$ to changes in growth rate. These relationships are visualized in
590　Figures 4B and 4C, in which the full solution space is indicated with black lines, but the permitted
591　solutions are defined by the regions over which the parameters yield both δ^2H values and growth-
592　rate slopes within error of the data (horizontal shaded areas). Exploration of this solution space
593　indicated the value of α_{TH} likely falls within the range of prior reports for soluble (sTH, $\alpha = 0.566$;
594　(Wijker et al., 2019)) and/or membrane bound (PntAB, maximum fractionation endmember $\alpha =$
595　0.222; (Jackson et al., 1999; Wijker et al., 2019)) transhydrogenases, and it makes little difference
596　to the model outcome if α_{TH} is constrained to any value between 0.222 to 0.566 (Table 4; see also
597　Figure S6C).
598
599　To further understand these results, a sensitivity analysis was performed by analyzing Eq. 13 for
600　its response to individual variables, while holding the others constant at the best fit predictions
601　(Figure 4). Among all the variables, the ^2H composition of BPs is most sensitive to α_{Fd}. Notably,
602　it also is more sensitive to λ than it is to α_{TH}, particularly to satisfy the requirement of minimal
603　sensitivity to growth rate. This sensitivity helps to further predict the likely value of α_{TH}. For
604　example, if λ is set to 0.04, the data are satisfied only by values of α_{TH} between 0.31 to 0.57, i.e.,
605　more similar to sTH than PntAB (Figure 4B). Alternatively, if α_{TH} is set to the mid-point (0.39),
606　the growth-rate slope limits λ to between 0.03 to 0.05. In comparison, the full model space allows
607　solutions for λ between 0.01 and 0.06.
608
609　Regardless, any reasonable estimate for α_{TH} implies the value of λ must be small, which is
610　consistent with the observation that $^2\varepsilon_{L/W}$ of *N. maritimus* biphytanes responds insignificantly to
611　changes in cell growth rate. Such a result also agrees with the concept that Archaea are optimized
612　for energy-limited conditions (Valentine, 2007), implying that nearly all reducing power (NADH
613　derived from the e^- donor) is allocated to obligatory cellular needs. At the estimate of $\lambda = 0.04$ and
614　a mid-point of $T_D = 56$ hr, the value of $f_N = 98\%$ (Eq. 8, 9), i.e., only 2% of produced NADH is
615　lost (f_L). A 98% value for f_N represents the electron flux that is harvested from NADH into the
616　NADPH pool and obligately dedicated to the full suite of cellular metabolic fates, only part of
617　which is lipid synthesis. If this conceptual framework is robust, it would be difficult to change the
618　isotopic composition of NADPH due to effects around the f_N vs. f_L branch point (Hayes, 2001),
619　and $^2\varepsilon_{L/W}$ should be very insensitive to growth rate, not only in AOA, but potentially in all
620　autotrophic archaea.
621
622　The final estimated solutions for Scenario 2 (Table 4) reproduce the three major features of the
623　$^2\varepsilon_{L/W}$ data for *N. maritimus* biphytanes: (*i*) highly ^2H-depleted absolute values, (*ii*) relative
624　insensitivity to changes in growth rate, and (*iii*) the increase in isotope ratio with ring number.

625   Specifically, the consensus model yields an increase of +6.7 ‰ per ring, compared to the +6.4 ‰
626   per ring observed for the data, and yields a small positive slope of $^2\varepsilon_{L/W}$ versus T_D (Figure 5). Most
627   of the ring-associated increase is attributed to the large KIE of the Fd reductant, while the relatively
628   shallow growth-rate slope reflects the small value of λ, which likely reflects inflexible
629   physiological fluxes in *N. maritimus*.
630
631

5. Discussion

633   The motivation for this work was to investigate the potential of $^2H/^1H$ ratios of archaeal lipids as
634   archives of past environments, ecologies, or physiologies. In sharp contrast to the > 600 ‰ range
635   of values observed across the bacteria, to-date the archaea stand out for their apparently narrow
636   span of $^2\varepsilon_{L/W}$ values. This is somewhat unexpected, given the diversity of species, growth
637   substrates, and metabolic strategies among the archaeal taxa studied to date (e.g., Kaneko et al.,
638   2011; Wu et al., 2020). Archaeal lipids appear always to be ^2H-depleted relative to growth water
639   and sit at the lower end of the range previously reported for bacterial fatty acids (Sessions et al.,
640   2002; Valentine et al., 2004; Campbell et al., 2009; Zhang et al., 2009; Heinzelmann et al., 2015;
641   Osburn et al., 2016; Leavitt et al., 2016; Leavitt et al., 2016; Leavitt et al., 2017).
642
643   Our results for *N. maritimus* show that BPs were generally more ^2H-depleted (-257 ‰ for BP-3 to
644   279 ‰ for BP-0) than the range of $^2\varepsilon_{L/W}$ values from the heterotrophic and halophilic archaeon
645   *Haloarcula marismortui*, which yielded archaeol/water fractionations of -103 to -228 ‰
646   (Dirghangi and Pagani, 2013), and batch cultures of hyperthermoacidophilic *Sulfolobus* spp.
647   (Kaneko et al., 2011; Lengger et al., 2021), from which BPs (raw, not relative to water) and
648   GDGTs/water were fractionated by -207 to -257 ‰ and *ca*. -180 ‰, respectively. The values we
649   observe for *N. maritimus* are similar to the range from *Methanosarcina barkerii*, which yielded
650   fractionations from -204 to -322 ‰ for phytanes/water, depending on methanogenesis substrate
651   (Wu et al., 2020). *N. maritimus* expresses simple patterns of $^2\varepsilon_{L/W}$ values, where the dominant
652   feature is a dependence on the number of rings, with the most ^2H-depleted values in BP-0 and the
653   least depleted in BP-3 (Figure 1). Mean total assemblage values of $^2\varepsilon_{L/W}$ show little sensitivity to
654   changes in growth rate as promoted by different fluxes of electron donor, especially when
655   compared to the fatty acids of bacteria grown with similar strategies (Kopf, 2015; Kopf et al.,
656   2015; Leavitt et al., 2019) The model developed above (Section 4) explored how these patterns
657   can help distinguish the H sources for BP biosynthesis and enabled estimation of the KIEs for the
658   various enzymatic steps.
659
660   The key attributes required by the model solution (Scenario 2) are a highly fractionating value of
661   ferredoxin-derived hydrides (α_{Fd}), a relatively less-fractionating value for NADH-NADPH
662   transhydrogenation processes (α_{TH}), and an aggregated electron donor flux (i.e., $\alpha_{NADPH} \bullet \alpha_{NADPH}$)

663   somewhat less fractionating than α_{TH}. The minimal growth rate sensitivity implies that *N.*
664   *maritimus* undergoes almost no change in cellular flux balance, regardless of having relatively fast
665   or slow growth. This implicates a constant baseline δ^2H signature as a feature of a relatively
666   imperturbable central energy metabolism. Stepping beyond this experimental and model
667   framework, we now look toward physiological inferences and paleoenvironmental applications.
668

5.1. Biochemical drivers of $^2\varepsilon_{\text{L/W}}$ patterns

5.1.1 Sources of cofactor hydrogen for lipid synthesis in 3HP/4HB Archaea

671   *N. maritimus* is an obligate chemoautotroph that utilizes the 3HP/4HB pathway for carbon fixation
672   (Kim et al., 2016; Bayer et al., 2019, Könneke et al., 2014). Because all biphytane-bound H in the
673   present experiments is strictly biosynthetic, rather than assimilated as part of an organic substrate,
674   the observed differences in $^2\varepsilon_{\text{L/W}}$ values between individual BPs (Figure 1) must be primarily due
675   to different KIEs associated with the hydride transfer reactions that recharge intracellular electron
676   donors. As such, the patterns we observed here may be expressed differently in heterotrophic
677   archaea or during mixotrophic growth.
678

679   In the model framework developed here, the overall mean value for $^2\varepsilon_{\text{L/W}}$ in *N. maritimus* reflects
680   primarily the expression of α_{E} (0.743; equivalent to ~ -260 ‰), while the ring-based differences
681   and growth-rate effects are controlled by the downstream flux balances and KIEs (λ, α_{TH}, α_{NADPH},
682   α_{Fd}). This implies that $^2\varepsilon_{\text{L/W}}$ likely would or should be expressed differently in heterotrophic
683   archaea. This may help to explain why our results are similar, yet not equal, to prior data from
684   *Haloarchula marismortui* and *Sulfolobus spp.* (Kaneko et al., 2011; Dirghangi and Pagani, 2013);
685   these prior data also were not obtained on steady-state cultures, which may be an additional factor
686   contributing to the observed differences. The only major catabolic enzyme in *N. maritimus* is
687   isocitrate dehydrogenase (ICT) in the TCA cycle, which we expect to be minimally expressed
688   (Könneke et al., 2014). However, in a range of heterotrophic aerobic archaea (e.g., *Sulfolobus*
689   species), not only this step, but more importantly glucose dehydrogenase from the Entner-
690   Doudoroff pathway should be a major NADPH contributor (Nunn et al., 2010; Bräsen et al., 2014),
691   potentially with an impact on the final $^2\varepsilon_{\text{L/W}}$ signature.
692

693   The most definitive result of our modeling approach (Section 4) is the prediction of a highly
694   fractionating KIE (α_{Fd}) for the e^- donor for GGR during saturation of DGGGP, which stands
695   separate from the above caveats. The *in vivo* electron donor for GGR is not yet known in *N.*
696   *maritimus*, but our inference of a specific role for ferredoxin-mediated reduction agrees with other
697   reports. To date there is no direct evidence that NADPH is used as the hydride donor for GGR in
698   archaea (Murakami et al., 2007; Sato et al., 2008). In contrast, observations from cyanobacteria
699   and plants (*Synechocystis* and *Arabidopsis* spp.) show GGR was directly reduced by NADPH
700   (Addlesee et al., 1996; Keller et al., 1998).
701

702   This raises the question: what is the major source of hydride to BP's in *N. maritimus*? The most
703   likely candidate appears to be ferredoxin-NADP$^+$ reductase (FNR; Figure 2A), which is highly
704   conserved among both the pelagic marine and the terrestrial AOAs – though may be absent in the
705   non-AOA Thaumarchaeota (Ren et al., 2019). This distribution may indicate reduction of Fd by
706   NADPH is common in some archaea (Aliverti et al., 2008), and suggests Fd may be a common or
707   even the dominant hydride donor in *N. maritimus*. More convincing evidence for the role of Fd in
708   isoprenyl chain saturation (Figure 3, step 10b) comes from the heterologous expression of
709   *Methanosarcina acetivorans* GGR in *E. coli*, where saturation of DGGGP only occurred when a
710   functional Fd from *M. acetivorans* was also provided (Isobe *et al.*, 2014). Although in an analogous
711   experiment on *S. acidocaldarius*, GGR was active without including a native Fd, the authors note
712   *E. coli* Fd was present and suggested it may have played a role. Alternatively, however, it appears
713   that some archaeal GGRs may utilize a NADH-flavin cofactor process for hydride transfer: *in vitro*
714   studies of GGRs from thermoacidophiles *Sulfolobus acidocaldarius* and *Thermoplasma*
715   *acidophilum* implicated this mechanism instead (Nishimura and Eguchi, 2006; Sasaki et al., 2011).
716
717   Although we specify the GGR reductant is NADPH-Fd (FNR; Figure 2), rather than NADH-flavin,
718   more work is needed to distinguish these two options. Our choice to invoke the former is based on
719   two arguments. First, it appears that ferredoxin-dependent and flavin-NAD complexes may be
720   favored in chemo(litho)autotrophs (Buckel and Thauer, 2018; Boyd et al., 2020). Second, there is
721   evidence that Fd co-factors could carry very large isotope effects into the donated H$^-$ pool. This
722   feature is a requirement to generate a relatively large (6.4 ‰) per-ring shift in $^2\varepsilon_{L/W}$. The strong
723   ^{2}H-depletion ($\alpha_{Fd} = 0.13$ to 0.14; -860 to -870 ‰; Table 4) we estimate for the GGR reductant may
724   be broadly consistent with prior estimates that fractionation of hydride donors to Fd and NADP$^+$
725   during photosynthesis in cyanobacteria are on the order of $\alpha = 0.43$ relative to water (Luo et al.,
726   1991), although this still falls considerably short of our predicted KIE for Fd. More promisingly,
727   direct rate assays for the two isotopes (k_{1H}/k_{2H}) using purified *Anabena sp.* FNR show values from
728   5.7 to 6.4 (4,700 to 5,400‰) due to hydrogen tunneling (Peregrina et al., 2010; Sánchez-Azqueta
729   et al., 2014). In general, these reports indicate large isotope fractionations during hydride transfers
730   that involve iron-sulfur clusters. Given the wide distribution of FNR in marine AOA, we therefore
731   suggest that it is both the most likely donor for GGR (thereby resembling *M. acetivorans*), and that
732   its KIE *in vivo* is likely to be highly fractionating. Regardless of specific carrier, however, our
733   model provides tight constraints on the ^{2}H/^{1}H signature of the GGR donor.
734
735   Regardless of any inferences about the hydride sources to GGR, synthesis of GDGTs also requires
736   hydrides donated directly from NADPH, both during synthesis of acetyl-CoA (Figure S4) and
737   later, during polyisoprene synthesis to yield DGGGP (Figure 3, steps 1-7). The core catabolic
738   pathway of ammonia oxidation in *N. maritimus* and other AOAs, however, likely generates NADH
739   via ferredoxin or FAD-dependent oxidoreductases interacting with Nuo = NDH1
740   (NADH:ubiquinone oxidoreductase) rather than NADPH (Walker et al., 2010; Qin et al., 2018;
741   Shafiee et al., 2022). It is unclear if Nuo can generate NADPH in AOAs. In case it cannot, this

742 necessitates *N. maritimus* to produce NADPH for anabolism by other means (Spaans et al., 2015)
743 such as via a yet unidentified transhydrogenase (as assumed in our metabolic model). A better
744 understanding of the precise mechanism(s) by which *N. maritimus* interconverts
745 NADH↔NADPH, or how it generates NADPH directly during catabolism, is central to
746 interpreting the $^2\varepsilon_{L/W}$ signatures encoded in its lipids. Similarly, these sources of lipid H will need
747 to be identified in all BP and GDGT synthesizing archaea in order to understand their lipid-H
748 isotope signatures.
749
750 In bacteria, the biosynthetic NADPH pool is regenerated by transhydrogenation from NADH, and
751 thus sources its reducing power directly from the primary supply generated by the electron
752 transport chain (Sauer et al., 2004; Fuhrer and Sauer, 2009). In most bacteria this process is
753 catalyzed by transhydrogenase (TH) enzymes that transfer the hydride (H$^-$) between NADH and
754 NADP$^+$ as needed to replenish deficits as NADPH hydrides are consumed during anabolism
755 (biosynthesis) (Sauer et al., 2004). The hydride transfer reaction by bacterial TH enzymes are
756 associated with a strong ^{2}H discrimination (ε_{TH} = -778 ‰ to -434 ‰; (Jackson et al., 1999; Wijker
757 et al., 2019)). While homologues of bacterial THs are seen in some methanogens, they are
758 otherwise rare in Archaea (c.f. (Buckel and Thauer, 2013, 2018; Leavitt et al., 2016; Poudel et al.,
759 2018). Consistent with this rarity, we were unable to find homologues to common bacterial (e.g.,
760 *E. coli* or *D. alaskensis*) soluble or membrane associated transhydrogenases in the *N. maritimus*
761 genome (Table S2). *N. maritimus*, like other archaea, does encode other mechanisms to balance
762 their intracellular redox budgets (Spaans et al., 2015; Boyd et al., 2020) and all NADPH producing
763 enzymes annotated in the *N. maritimus* genome are summarized in Table S2. The main NADPH
764 sources not associated with central carbon metabolism include a cytosolic NADP+-reducing
765 hydrogenase (SH; Nmari_0253, Nmar_0267, Nmar_1389), and the aforementioned
766 ferredoxin:NADP+ oxidoreductase (FNR; Nmar_0672). Sources of NADPH coupled to the TCA
767 cycle is the IDH (Nmar_1069, Nmar_1379) mentioned above, and coupled to the non-
768 phosphorylating Entner Doudoroff pathway is a NADP+ glyceraldehyde dehydrogenase
769 (Nmari_1608). Given the lack of transhydrogenase identified in the SCM1 genome, and the other
770 sources, the main NADPH producing mechanism of note is FNR, with its predicted large
771 fractionation.
772
773 From the isotopic perspective, our $^2\varepsilon_{L/W}$ data appear to be consistent with the picture that has
774 emerged from bacterial transhydrogenases. That is, the known KIE associated with bacterial
775 NADPH/NADH hydride transfer is strongly fractionating (Table 4), but is not as ^{2}H-depleted as
776 hydrides supplied by Fd via FNR. Regardless, our model is not very sensitive to the value chosen
777 for α_{TH}, since it simply couples a stronger fractionation (smaller assigned α_{TH}) to a lower degree
778 of "leakiness" (smaller λ) or the converse (less fractionating α_{TH} with larger λ) to achieve equal
779 goodness of fit (Figure 5). It is therefore more informative to note that this approach places hard
780 constraints on the maximum value of λ and indicates there are no permitted solutions that enable
781 significant energy waste (lost NADH, f_L) in *N. maritimus*. It also appears unlikely that the process

782   identified here (generation of f_N with α_{TH}) is somehow the same as that symbolized by the f_{Fd}
783   contribution, i.e., the lack of overlap between estimates for α_{TH} and α_{Fd} indicates two unique
784   sources of reducing hydrides are required, even if in the present configuration we have identified
785   them incorrectly.
786
787   **5.1.2. Interpreting metabolic limits on $^2\varepsilon_{L/W}$ values**
788   In the framework set forth by Wijker et al. (2019) for bacteria, *N. maritimus* would be operating
789   near the NADPH imbalance flux approaching -100% (see Wijker et al. (2019) Figure 3). Although
790   the notation between our model and theirs is different, our best fit estimate for $\lambda = 0.04$ (range 0.01
791   to 0.06; Table 4) equates to a balance around NADH where 98% of the electron flux is required
792   for NADPH generation and only 2% is in "excess" for recycling or leakage. This places *N.*
793   *maritimus* at -98% NADPH imbalance in the Wijker et al. (2019) reference frame (Figure 6).
794
795   The maximum H isotope fractionation for average BPs relative to water can be inferred from
796   Figure 6 by extrapolating to -100% NADPH, yielding an intercept of -282 ‰. It remains unknown
797   whether this also is a reasonable approximate minimum value for $^2\varepsilon_{L/W}$ for bacterial production,
798   or whether the ~ 200‰ scatter in the vertical dimension in Figure 7 portends a similar range for
799   the projected minima of diverse organisms. A possibility that requires further investigation is
800   whether free energy differences, i.e., impacts on α_E, are primarily responsible for changes in $^2\varepsilon_{L/W}$
801   at a given NADPH imbalance (changes in the vertical), while changes in flux balance, growth rate,
802   and overall energy demand set this imbalance. If so, more experiments at constant energy flux for
803   organisms with distinct metabolisms will help define this space, and the outcome of inferred α_E
804   may reflect thermodynamic properties of the experiments. Any potential contributions from
805   equilibrium isotope exchange in various reaction steps also remain unknown. Such effects could
806   be examined by cultivation at different temperatures, although likely with a different taxon (*N.*
807   *maritimus* is grown isothermally at 28 °C). Thus, while we do not know how the observed $^2\varepsilon_{L/W}$
808   we observed at 28 °C relates to the maximum KIE of a unidirectional hydride (H⁻) donation, or
809   whether there is H⁻ isotopic exchange at equilibrium, we can infer that considerable kinetic
810   expression is required (also justifying our exclusion of Scenarios 3 and 4 in the original model).
811   Theoretical calculations of the equilibrium isotope effect (EIE) for an idealized isoprenoid vs.
812   water yielded an estimate of -100 ‰, which was essentially insensitive to temperature over a range
813   of 0 to 100 °C (Wang et al., 2009). This is effectively the same as what we assigned empirically
814   for the water KIE ($\alpha_W = 0.9$) and suggests the water-derived KIE component of BP biosynthesis
815   will not respond to temperature variations. Together these examples imply that the $^2\varepsilon_{L/W}$ signals of
816   Thaumarchaeota BPs are unlikely to be temperature-sensitive, in addition to their insensitivity to
817   growth rate.
818

819   **5.2. Applications**

820   **5.2.1 Calibrating biphytane $^2\varepsilon_{L/W}$ offsets for paleohydrology and paleoecology**

821   Archaeal lipids may offer some unique advantages as H isotope proxies. The iGDGTs found in
822   aquatic sediments are believed to derive predominantly from marine or lacustrine ammonia-
823   oxidizing Thaumarchaeota living in the overlying water column (Powers *et al.*, 2010; Pearson and
824   Ingalls, 2013, Schouten et al., 2013). This contrasts with leaf wax-derived *n*-alkanes, which can
825   derive from a complex plant community, may have both terrestrial and aquatic sources, and
826   production is seasonally-biased in some regions (Gao et al., 2011; Sachse et al., 2012; McFarlin et
827   al., 2019). The larger diversity of $^2\varepsilon_{L/W}$ values expressed by *n*-alkanes reflects both the diversity of
828   the local ecosystem and this source-transport signal (Sachse et al., 2012; Gao et al., 2014). In
829   lacustrine bodies with minimal terrigenous overpriting, it may be possible to reconstruct the water
830   δ^2H composition from archaeal biphytanes and an estimated constant $^2\varepsilon_{L/W}$ value, using either a
831   mean value or individual BP-specific values. Tandem work on modern lake core-tops over a range
832   of temperature regimes may provide an indication of the magnitude of any temperature effects,
833   though it remains unknown whether this archaeal $^2\varepsilon_{L/W}$ offset is temperature sensitive (*see* section
834   5.1.2). Once calibrated, the reconstructed lake water record could be compared to estimated
835   regional meteoric water δ^2H values obtained from co-deposited *n*-alkanes that reflect water
836   available to the surrounding vegetation during the period of leaf synthesis (Tipple et al., 2013),
837   potentially yielding insights to past changes in the hydrologic cycle or plant physiological effects
838   that can be missing from the plant perspective (Sachse et al., 2012), and may help unpack diverse
839   GDGT sources in some lacustrine systems when paired with C-isotopes (Sinninghe Damsté et al.,
840   2022). In the marine environment, variation in the δ^2H value of ocean water is minimal, and a
841   modern core-top calibration would serve to uniquely calibrate temperature signals independently
842   from variations in source water. Both types of calibration efforts likely will be needed.

843

844   Variations in salinity have *ca.* 50 ‰ effects on the $^2\varepsilon_{L/W}$ values of alkenones from haptophyte algae
845   (Schouten et al., 2006; van der Meer et al., 2015; Sachs et al., 2016). The mechanism by which
846   salinity affects $^2\varepsilon_{L/W}$ values in haptophytes remains unclear, but it has been hypothesized that such
847   effects may be restricted to photoautotrophs (Heinzelmann et al., 2015a). Differences in salinity
848   and taxonomy produce different iGDGT assemblages among Thaumarchaeota (Elling et al., 2015;
849   2017), which would then yield differences between taxa in their bulk average $^2\varepsilon_{L/W}$ values to be
850   consistent with the pattern of increasing $^2\varepsilon_{L/W}$ for BP-0…BP-3. However, estimates of the net
851   effect of such changes based on variation in Ring Index suggests that the effect would be minimal
852   (< 10 ‰), even between the very high Ring Index composition of *Nitrososphaera gargensis* (BP-
853   0:1:2:3 ratio of 0.02:0.02:0.51:0.45; calculated by Elling and colleagues by assuming iGDGT-2
854   consists only of 2 x BP-1 (Elling et al., 2017)) vs. the BP distribution in *N. maritimus*. Thus, the
855   taxonomic influence of iGDGT compositional changes on average $^2\varepsilon_{L/W}$ should be insignificant.
856   Whether $^2\varepsilon_{L/W}$ values are influenced by salinity independently of changes in ring distribution
857   requires further investigation. It may be likely that regional temperature calibrations would
858   overwhelm any salinity effects or taxonomic community shifts in the evaluation of either lacustrine

859   or marine biphytane δ^2H proxies. For applications in lacustrine or riverine sediments, salinity is of

860   no concern, but alternatively, proxies in these settings should be examined for potential pH effects.

861

862   Growth rates of natural microbial communities can vary spatially and temporally, depending on

863   the availability of nutrients, electron donors and acceptors, temperature, and other environmental

864   parameters. The conditions used in this work were designed to test a broad range of metabolic rates

865   at controlled steady state. We anticipated that variations in energy budgets associated with fast and

866   slow growth would yield heterogeneity of $^2\varepsilon_{L/W}$ values analogous to the differences in $^2\varepsilon_{L/W}$ values

867   of bacteria grown aerobically on different hexoses (Wijker et al., 2019), or haptophyte algae grown

868   at different rates by varying the temperature (Schouten et al., 2006) or nutrient supply (Sachs and

869   Kawka, 2015). Instead, we observed a nearly zero growth rate effect on expression of $^2\varepsilon_{L/W}$ in $N.$

870    $maritimus$ despite using a 3-fold range of doubling time that is believed to encompass most of the

871   natural conditions of marine AOA (e.g., (Santoro and Casciotti, 2011; Qin et al., 2014)). The

872   direction of this response is the same as for haptophyte algae, with a decrease in $^2\varepsilon_{L/W}$ (i.e., greater

873   fractionation) observed at faster growth rates, but with a magnitude significantly less than what

874   was observed for lipids of algae grown in chemostats (Sachs and Kawka, 2015). Previous work on

875    $Haloarcula\ marismortui$ (a halophilic archaea) showed variations in $^2\varepsilon_{L/W}$ values up to 25 ‰

876   between fastest and slowest growth (T_D from 8 to 16 h; (Dirghangi and Pagani, 2013). However,

877   because the halophile work was done in batch culture, these doubling times reflect non-constant

878   growth rates and integrate across the culture's growth stages, making direct comparison to our

879   steady-state experiments difficult. We suggest that the highest growth-rate sensitivity for $^2\varepsilon_{L/W}$

880   values of archaea likely would be expressed in cultures cultivated at maximum free energy (e.g.,

881   aerobically on simple sugars), and that studies in aerobic heterotrophs are necessary to confirm

882   this endmember. Environmental conditions likely would be more constrained, and accordingly

883   there should be less growth-rate variability in $^2\varepsilon_{L/W}$ for natural archaeal communities, and

884   especially for those that are autotrophic like the ammonia-oxidizing Thaumarchaeota.

885

886   Collectively our data support the idea that a unifying feature of the archaea is the operation of

887   maximally energy-efficient metabolisms (Valentine, 2007). This is reflected by highly fractionated

888   lipid δ^2H values, which are consistent with an overall metabolic status of having just enough

889   NADPH or other internal electron donor to meet cellular demand (Wijker et al., 2019). We would

890   further suggest that the inability to shift $^2\varepsilon_{L/W}$ values off this minimum in $N.\ maritimus$, even when

891   supplying electron donor at an increased rate, indicates the marine Thaumarchaeota have

892   inherently stable internal fluxes that were selected for during their adaptation to extreme

893   oligotrophy (Martens-Habbena et al., 2009). This would be consistent with supply-side control of

894   the rate of archaeal metabolism (Amenabar et al., 2017). Unless growth temperature has a

895   significant impact, marine and lacustrine autotrophic Thaumarchaeota will have reliably invariant

896    $^2H/^1H$ fractionation regardless of growth rate, nutrient status, or differences in community

897   composition, and the environmental expression of archaeal $^2\varepsilon_{L/W}$ should be more constant than for

898   marine algae.

899

5.2.2. Distinguishing iGDGT sources using stable isotope patterns of biphytanes

Combining carbon and hydrogen isotope analyses of sedimentary biphytanes may provide a powerful new means to disentangle sources and processes. In marine systems, compound distributions and carbon isotopic measurements indicate sedimentary iGDGTs appear to be derived mostly from local planktonic sources (Shah et al., 2008; Pearson et al., 2016; Zhang et al., 2016). Easily detectable exceptions are cases where methane cycling has affected the $\delta^{13}C$ ratios and iGDGT profiles of the sedimentary lipid pool (e.g., (Sinninghe Damsté et al., 2001; Wakeham et al., 2003; Hoffmann-Sell et al., 2011; Zhang et al., 2011). However, the resolution of $\delta^{13}C$ isotope ratio mass balance estimates is relatively coarse, and radiocarbon measurements can be logistically difficult to acquire in sufficient numbers to yield definitive conclusions. There are many instances of minor deviations in Ring Index (Zhang et al., 2016) or small but consistent differences between $\delta^{13}C$ values of iGDGTs – particularly the notable ^{13}C offset of ca. 1 ‰ between iGDGT-0 and crenarchaeol that occurs in many marine sediments (Pearson et al., 2016; Polik et al., 2018; Elling et al., 2019) – that require better understanding. Whether these signals are simply noise (e.g., due to sediment mixing or other factors), or whether they reflect systematic differences in sedimentary sources, is critical to the interpretation of iGDGT proxies such as the widely applied TEX_{86} sea-surface temperature proxy (Schouten et al., 2002). Such signals may be diagnosable through δ^2H analysis of individual BPs.

918

The capacity to produce cyclopentyl-ring containing iGDGTs is widely distributed among the archaea (Zeng et al., 2019), but the cyclohexyl ring-containing iGDGT, crenarchaeol, is believed to be unique to the Thaumarchaeota (Pearson and Ingalls, 2013; Schouten et al., 2013). The iGDGTs in marine and lacustrine sediments therefore have the potential to integrate multiple sources, such that even if the dominant source is export of planktonic AOA, there also may be cases of significant input of benthic, soil-derived, or other allochthonous lipids. The distinctive pattern in relative $^2\varepsilon_{L/W}$ values between BP chains of a single source could serve as an isotopic fingerprint to identify the contribution of these multiple iGDGT sources to sedimentary archives. BPs obtained from any sediment in which the archaeal lipids reflect a homogeneous community growing in a common body of water should have equal $\delta^{13}C$ values (Hurley et al., 2019), as well as predictable differences in δ^2H values that conform to the pattern BP-0 < BP-1 < BP-2 < BP-3. Of these, the unique cyclohexane-containing BP-3 from crenarchaeol would serve as the anchor point for the planktonic signal.

932

A further advantage of this dual-stable isotope approach is the ability to obtain both sets of measurements (plus the overall iGDGT profile and the TEX_{86} ratio) from the same sample. This subverts the challenges of other multi-proxy approaches that may require comparison of lipid extracts to solid phases (e.g., elemental analyses for soil Al/Ti). Archaeal lipids from terrestrial freshwater environments are likely to be more depleted in ^2H than those produced in seawater, with a differential that increases with latitude. Similarly, $\delta^{13}C$ values of archaeal BPs from

continental sources may be either more negative or more variable than marine waters (Weijers et al., 2009; Lattaud et al., 2021). Dual C and H isotope patterns for BPs may prove particularly useful to diagnose terrestrial iGDGT inputs to marine sediments, thereby adding to the distribution metrics such as Ring Index, Methane Index, iGDGT-2/3 ratio, and other profiling strategies (Zhang et al., 2011, 2016; Taylor et al., 2013; Dunkley Jones et al., 2020) that currently are used to assess fidelity of the TEX_{86} index. Furthermore, the archaeal lipid-H proxy may be useful in tracking past climate through events such as the PETM in terrestrial records, and perhaps more recent shifts in the Plio-Plistocene and Holocene.

5.3 Summary

In this study we quantified the hydrogen isotope fractionation between growth water and lipids in a well-studied strain of the ubiquitous marine ammonium oxidizing archaea in response to different steady-state electron donor fluxes. We observed little sensitivity to growth rate and a consistent pattern in the ordering of isotope fractionation with biphytane ring number. These observations are captured well in a bio-isotopic model, despite limited literature available on the intracellular hydride and electron carriers in environmentally important archaea. From the model, it is clear chemoautotrophic archaea, such as *N. maritimus,* add hydrides to the isoprenoid chains of GDGTs from a strongly depleted intracellular reservoir of NADPH. Moreover, *N. maritimus* cells in particular operate at near constant NADPH deficit as compared to previously studied bacteria. We extend the recent modelling approach of Wijker et al. (2019) to the Domain Archaea, and propose this framework is universal to microorganisms. Further experimental work within the archaea, both in aerobic chemolithotrophs such as the AOAs, as well as in anaerobic chemolithotrophs and aerobic and anaerobic heterotrophs, is necessary to determine how universal the lipid-water fractionation response is in the Archaea. These and subsequent experimental studies will determine how useful archaeal lipid hydrogen isotopes will be for use in paleohydrology and paleoecology.

6. Acknowledgments

7. Data & Model availability: https://github.com/KopfLab/2022_leavitt_et_al.

7. References

Addlesee H. A., Gibson L. C., Jensen P. E. and Hunter C. N. (1996) Cloning, sequencing and functional assignment of the chlorophyll biosynthesis gene, chlP, of Synechocystis sp. PCC 6803. *FEBS letters* **389**, 126–130.

Aliverti A., Pandini V., Pennati A., de Rosa M. and Zanetti G. (2008) Structural and functional diversity of ferredoxin-NADP+ reductases. *Archives of Biochemistry and Biophysics* **474**, 283–291.

Amenabar M. J., Shock E. L., Roden E. E., Peters J. W. and Boyd E. S. (2017) Microbial substrate preference dictated by energy demand rather than supply. *Nature geoscience* **10**, 577–581.

Bayer B., Pelikan C., Bittner M. J., Reinthaler T., Könneke M., Herndl G. J. and Offre P. (2019) Proteomic response of three marine ammonia-oxidizing archaea to hydrogen peroxide and their metabolic interactions with a heterotrophic alphaproteobacterium. *Msystems* **4**, e00181-19.

Bender A. L. D., Suess M., Chitwood D. H. and Bradley A. S. (2016) Investigating genetic loci that encode plant-derived paleoclimate proxies. In pp. PP24B-03.

Boyd E. S., Hamilton T. L., Wang J., He L. and Zhang C. L. (2013) The Role of Tetraether Lipid Composition in the Adaptation of Thermophilic Archaea to Acidity. *Front. Microbiol.* **4**.

Boyd E. S., Pearson A., Pi Y., Li W.-J., Zhang Y. G., He L., Zhang C. L. and Geesey G. G. (2011) Temperature and pH controls on glycerol dibiphytanyl glycerol tetraether lipid composition in the hyperthermophilic crenarchaeon Acidilobus sulfurireducens. *Extremophiles* **15**, 59–65.

Bräsen C., Esser D., Rauch B. and Siebers B. (2014) Carbohydrate metabolism in Archaea: current insights into unusual enzymes and pathways and their regulation. *Microbiology and Molecular Biology Reviews* **78**, 89–175.

Buckel W. and Thauer R. K. (2013) Energy conservation via electron bifurcating ferredoxin reduction and proton/Na+ translocating ferredoxin oxidation. *Biochimica et Biophysica Acta (BBA)-Bioenergetics* **1827**, 94–113.

Buckel W. and Thauer R. K. (2018) Flavin-based electron bifurcation, ferredoxin, flavodoxin, and anaerobic respiration with protons (Ech) or NAD+ (Rnf) as electron acceptors: A historical review. *Frontiers in microbiology* **9**, 401.

Campbell B. J., Li C., Sessions A. L. and Valentine D. L. (2009) Hydrogen isotopic fractionation in lipid biosynthesis by H2-consuming Desulfobacterium autotrophicum. *Geochimica et Cosmochimica Acta* **73**, 2744–2757.

Campbell B. J., Sessions A. L., Fox D. N., Paul B. G., Qin Q., Kellermann M. Y. and Valentine D. L. (2017) Minimal influence of [NiFe] hydrogenase on hydrogen isotope fractionation in H2-oxidizing cupriavidus necator. *Frontiers in microbiology* **8**, 1886.

Chen A., Dale Poulter C. and Kroon P. A. (1994) Isoprenyl diphosphate synthases: protein sequence comparisons, a phylogenetic tree, and predictions of secondary structure. *Protein Science* **3**, 600–607.

Chen A. and Poulter C. (1993) Purification and characterization of farnesyl diphosphate/geranylgeranyl diphosphate synthase. A thermostable bifunctional enzyme from Methanobacterium thermoautotrophicum. *Journal of Biological Chemistry* **268**, 11002–11007.

1022   Cobban A., Zhang Y., Zhou A., Weber Y., Elling F. J., Pearson A. and Leavitt W. D. (2020)
1023   Multiple environmental parameters impact lipid cyclization in Sulfolobus acidocaldarius.
1024   *Environmental Microbiology* **22**, 4046–4056.
1025   Dawson K. S., Osburn M. R., Sessions A. L. and Orphan V. J. (2015) Metabolic associations
1026   with archaea drive shifts in hydrogen isotope fractionation in sulfate-reducing bacterial
1027   lipids in cocultures and methane seeps. *Geobiology* **13**, 462–477.
1028   Dirghangi S. S. and Pagani M. (2013) Hydrogen isotope fractionation during lipid biosynthesis
1029   by Haloarcula marismortui. *Geochimica et Cosmochimica Acta* **119**, 381–390.
1030   Dunkley Jones T., Eley Y. L., Thomson W., Greene S. E., Mandel I., Edgar K. and Bendle J. A.
1031   (2020) OPTiMAL: a new machine learning approach for GDGT-based
1032   palaeothermometry. *Climate of the Past* **16**, 2599–2617.
1033   Elling F. J., Gottschalk J., Doeana K. D., Kusch S., Hurley S. J. and Pearson A. (2019) Archaeal
1034   lipid biomarker constraints on the Paleocene-Eocene carbon isotope excursion. *Nature
1035   communications* **10**, 1–10.
1036   Elling F. J., Könneke M., Nicol G. W., Stieglmeier M., Bayer B., Spieck E., de la Torre J. R.,
1037   Becker K. W., Thomm M. and Prosser J. I. (2017) Chemotaxonomic characterisation of
1038   the thaumarchaeal lipidome. *Environmental microbiology* **19**, 2681–2700.
1039   Estep M. F. and Hoering T. C. (1980) Biogeochemistry of the stable hydrogen isotopes.
1040   *Geochimica et Cosmochimica Acta* **44**, 1197–1206.
1041   Feyhl-Buska J., Chen Y., Jia C., Wang J.-X., Zhang C. L. and Boyd E. S. (2016) Influence of
1042   growth phase, pH, and temperature on the abundance and composition of tetraether lipids
1043   in the Thermoacidophile Picrophilus torridus. *Frontiers in microbiology* **7**, 1323.
1044   Fuhrer T. and Sauer U. (2009) Different biochemical mechanisms ensure network-wide
1045   balancing of reducing equivalents in microbial metabolism. *Journal of bacteriology* **191**,
1046   2112–2121.
1047   Gao L., Hou J., Toney J., MacDonald D. and Huang Y. (2011) Mathematical modeling of the
1048   aquatic macrophyte inputs of mid-chain n-alkyl lipids to lake sediments: Implications for
1049   interpreting compound specific hydrogen isotopic records. *Geochimica et Cosmochimica
1050   Acta* **75**, 3781–3791.
1051   Gao L., Zheng M., Fraser M. and Huang Y. (2014) Comparable hydrogen isotopic fractionation
1052   of plant leaf wax n-alkanoic acids in arid and humid subtropical ecosystems.
1053   *Geochemistry, Geophysics, Geosystems* **15**, 361–373.
1054   Gat J. R. (1996) Oxygen and hydrogen isotopes in the hydrologic cycle. *Annual Review of Earth
1055   and Planetary Sciences* **24**, 225–262.
1056   Hayakawa H., Motoyama K., Sobue F., Ito T., Kawaide H., Yoshimura T. and Hemmi H. (2018)
1057   Modified mevalonate pathway of the archaeon Aeropyrum pernix proceeds via trans-
1058   anhydromevalonate 5-phosphate. *Proceedings of the National Academy of Sciences* **115**,
1059   10034–10039.
1060   Hayes J. (2001) Fractionation of the isotopes of carbon and hydrogen in biosynthetic processes,
1061   pp. 225Ð277. *Stable isotope geochemistry* **43**.
1062   Heinzelmann S. M., Chivall D., M'Boule D., Sinke-Schoen D., Villanueva L., Damsté J. S. S.,
1063   Schouten S., Van der Meer M. T. and Oren A. (2015a) Comparison of the effect of
1064   salinity on the D/H ratio of fatty acids of heterotrophic and photoautotrophic
1065   microorganisms. *FEMS microbiology letters* **362**.
1066   Heinzelmann S. M., Villanueva L., Lipsewers Y. A., Sinke-Schoen D., Damste J. S. S., Schouten
1067   S. and van der Meer M. T. (2018) Assessing the metabolism of sedimentary microbial

1068   communities using the hydrogen isotopic composition of fatty acids. *Organic*
1069   *Geochemistry* **124**, 123–132.
1070 Heinzelmann S. M., Villanueva L., Sinke-Schoen D., Sinninghe Damsté J. S., Schouten S. and
1071   Van der Meer M. T. (2015b) Impact of metabolism and growth phase on the hydrogen
1072   isotopic composition of microbial fatty acids. *Frontiers in microbiology* **6**, 408.
1073 Hoffmann-Sell L., Birgel D., Arning E. T., Föllmi K. B. and Peckmann J. (2011) Archaeal lipids
1074   in Neogene dolomites (Monterey and Sisquoc Formations, California)–Planktic versus
1075   benthic archaeal sources. *Organic geochemistry* **42**, 593–604.
1076 Hou J., D'Andrea W. J. and Huang Y. (2008) Can sedimentary leaf waxes record D/H ratios of
1077   continental precipitation? Field, model, and experimental assessments. *Geochimica et*
1078   *Cosmochimica Acta* **72**, 3503–3517.
1079 Hurley S. J., Elling F. J., Könneke M., Buchwald C., Wankel S. D., Santoro A. E., Lipp J. S.,
1080   Hinrichs K.-U. and Pearson A. (2016) Influence of ammonia oxidation rate on
1081   thaumarchaeal lipid composition and the TEX86 temperature proxy. *Proceedings of the*
1082   *National Academy of Sciences* **113**, 7762–7767.
1083 Isobe K., Ogawa T., Hirose K., Yokoi T., Yoshimura T. and Hemmi H. (2014) Geranylgeranyl
1084   Reductase and Ferredoxin from Methanosarcina acetivorans Are Required for the
1085   Synthesis of Fully Reduced Archaeal Membrane Lipid in Escherichia coli Cells. *Journal*
1086   *of Bacteriology* **196**, 417–423.
1087 Jackson J. B., Peake S. J. and White S. A. (1999) Structure and mechanism of proton-
1088   translocating transhydrogenase. *FEBS letters* **464**, 1–8.
1089 Jain S., Caforio A. and Driessen A. J. (2014) Biosynthesis of archaeal membrane ether lipids.
1090   *Frontiers in microbiology* **5**, 641.
1091 Kahmen A., Dawson T. E., Vieth A. and Sachse D. (2011) Leaf wax n-alkane δD values are
1092   determined early in the ontogeny of Populus trichocarpa leaves when grown under
1093   controlled environmental conditions. *Plant, Cell & Environment* **34**, 1639–1651.
1094 Kaneko M., Kitajima F. and Naraoka H. (2011) Stable hydrogen isotope measurement of
1095   archaeal ether-bound hydrocarbons. *Organic Geochemistry* **42**, 166–172.
1096 Keller Y., Bouvier F., d'Harlingue A. and Camara B. (1998) Metabolic compartmentation of
1097   plastid prenyllipid biosynthesis: evidence for the involvement of a multifunctional
1098   geranylgeranyl reductase. *European Journal of Biochemistry* **251**, 413–417.
1099 Kellermann M. Y., Yoshinaga M. Y., Wegener G., Krukenberg V. and Hinrichs K.-U. (2016)
1100   Tracing the production and fate of individual archaeal intact polar lipids using stable
1101   isotope probing. *Organic Geochemistry* **95**, 13–20.
1102 Kim J.-G., Park S.-J., Damsté J. S. S., Schouten S., Rijpstra W. I. C., Jung M.-Y., Kim S.-J.,
1103   Gwak J.-H., Hong H. and Si O.-J. (2016) Hydrogen peroxide detoxification is a key
1104   mechanism for growth of ammonia-oxidizing archaea. *Proceedings of the National*
1105   *Academy of Sciences* **113**, 7888–7893.
1106 Kim J.-H., Schouten S., Hopmans E. C., Donner B. and Damsté J. S. S. (2008) Global sediment
1107   core-top calibration of the TEX86 paleothermometer in the ocean. *Geochimica et*
1108   *Cosmochimica Acta* **72**, 1154–1173.
1109 Kim J.-H., Van der Meer J., Schouten S., Helmke P., Willmott V., Sangiorgi F., Koç N.,
1110   Hopmans E. C. and Damsté J. S. S. (2010) New indices and calibrations derived from the
1111   distribution of crenarchaeal isoprenoid tetraether lipids: Implications for past sea surface
1112   temperature reconstructions. *Geochimica et Cosmochimica Acta* **74**, 4639–4654.

1113   Koga Y. and Morii H. (2007) Biosynthesis of ether-type polar lipids in archaea and evolutionary
1114   considerations. *Microbiology and Molecular Biology Reviews* **71**, 97–120.
1115   Könneke M., Bernhard A. E., José R., Walker C. B., Waterbury J. B. and Stahl D. A. (2005)
1116   Isolation of an autotrophic ammonia-oxidizing marine archaeon. *Nature* **437**, 543–546.
1117   Könneke M., Schubert D. M., Brown P. C., Hügler M., Standfest S., Schwander T., von
1118   Borzyskowski L. S., Erb T. J., Stahl D. A. and Berg I. A. (2014) Ammonia-oxidizing
1119   archaea use the most energy-efficient aerobic pathway for CO2 fixation. *Proceedings of*
1120   *the National Academy of Sciences* **111**, 8239–8244.
1121   Kopf S., Davidheiser-Kroll B. and Kocken I. (2021) Isoreader: An R package to read stable
1122   isotope data files for reproducible research. *Journal of Open Source Software* **6**, 2878.
1123   Kopf S. H. (2015) From lakes to lungs: Assessing microbial activity in diverse environments.
1124   Kopf S. H., McGlynn S. E., Green-Saxena A., Guan Y., Newman D. K. and Orphan V. J. (2015)
1125   Heavy water and 15 N labelling with N ano SIMS analysis reveals growth rate-dependent
1126   metabolic heterogeneity in chemostats. *Environmental microbiology* **17**, 2542–2556.
1127   Kreuzer-Martin H. W., Lott M. J., Ehleringer J. R. and Hegg E. L. (2006) Metabolic processes
1128   account for the majority of the intracellular water in log-phase Escherichia coli cells as
1129   revealed by hydrogen isotopes. *Biochemistry* **45**, 13622–13630.
1130   Lattaud J., De Jonge C., Pearson A., Elling F. J. and Eglinton T. I. (2021) Microbial lipid
1131   signatures in Arctic deltaic sediments–Insights into methane cycling and climate
1132   variability. *Organic Geochemistry* **157**, 104242.
1133   Leavitt William D., Flynn T. M., Suess M. K. and Bradley A. S. (2016) Transhydrogenase and
1134   Growth Substrate Influence Lipid Hydrogen Isotope Ratios in Desulfovibrio alaskensis
1135   G20. *Frontiers in Microbiology* **07**.
1136   Leavitt W. D., Murphy S. J.-L., Lynd L. R. and Bradley A. S. (2017) Hydrogen isotope
1137   composition of Thermoanaerobacterium saccharolyticum lipids: Comparing wild type
1138   with a nfn- transhydrogenase mutant. *Organic Geochemistry* **113**, 239–241.
1139   Leavitt William D, Venceslau S. S., Pereira I. A., Johnston D. T. and Bradley A. S. (2016)
1140   Fractionation of sulfur and hydrogen isotopes in Desulfovibrio vulgaris with perturbed
1141   DsrC expression. *FEMS microbiology letters* **363**.
1142   Leavitt W. D., Venceslau S. S., Waldbauer J., Smith D. A., Pereira I. A. C. and Bradley A. S.
1143   (2019) Proteomic and isotopic response of Desulfovibrio vulgaris to DsrC perturbation.
1144   *Frontiers in microbiology* **10**, 658.
1145   Lengger S. K., Weber Y., Taylor K. W., Kopf S. H., Berstan R., Bull I. D., Mayser J., Leavitt W.
1146   D., Blewett J. and Pearson A. (2021) Determination of the δ2H values of high molecular
1147   weight lipids by high-temperature gas chromatography coupled to isotope ratio mass
1148   spectrometry. *Rapid Communications in Mass Spectrometry* **35**, e8983.
1149   Liu H., Cao Y., Hu J., Liu Z. and Liu W. (2022) Substantial peak size effect on compound-
1150   specific δD values analyzed on isotope ratio mass spectrometry. *Chemical Geology*,
1151   120721.
1152   Luo Y.-H., Steinberg L., Suda S., Kumazawa S. and Mitsui A. (1991) Extremely low D/H ratios
1153   of photoproduced hydrogen by cyanobacteria. *Plant and cell physiology* **32**, 897–900.
1154   Maloney A. E., Shinneman A. L., Hemeon K. and Sachs J. P. (2016) Exploring lipid 2H/1H
1155   fractionation mechanisms in response to salinity with continuous cultures of the diatom
1156   Thalassiosira pseudonana. *Organic Geochemistry* **101**, 154–165.

1157   Martens-Habbena W., Berube P. M., Urakawa H., José R. and Stahl D. A. (2009) Ammonia
1158   oxidation kinetics determine niche separation of nitrifying Archaea and Bacteria. *Nature*
1159   **461**, 976–979.
1160   McFarlin J. M., Axford Y., Masterson A. L. and Osburn M. R. (2019) Calibration of modern
1161   sedimentary δ2H plant wax-water relationships in Greenland lakes. *Quaternary Science*
1162   *Reviews* **225**, 105978.
1163   McInerney F. A., Helliker B. R. and Freeman K. H. (2011) Hydrogen isotope ratios of leaf wax
1164   n-alkanes in grasses are insensitive to transpiration. *Geochimica et Cosmochimica Acta*
1165   **75**, 541–554.
1166   van der Meer M. T., Benthien A., French K. L., Epping E., Zondervan I., Reichart G.-J., Bijma
1167   J., Damsté J. S. S. and Schouten S. (2015) Large effect of irradiance on hydrogen isotope
1168   fractionation of alkenones in Emiliania huxleyi. *Geochimica et Cosmochimica Acta* **160**,
1169   16–24.
1170   Murakami M., Shibuya K., Nakayama T., Nishino T., Yoshimura T. and Hemmi H. (2007)
1171   Geranylgeranyl reductase involved in the biosynthesis of archaeal membrane lipids in the
1172   hyperthermophilic archaeon Archaeoglobus fulgidus. *The FEBS journal* **274**, 805–814.
1173   Nishimura Y. and Eguchi T. (2006) Biosynthesis of archaeal membrane lipids:
1174   digeranylgeranylglycerophospholipid reductase of the thermoacidophilic archaeon
1175   Thermoplasma acidophilum. *Journal of biochemistry* **139**, 1073–1081.
1176   Nunn C. E., Johnsen U., Schönheit P., Fuhrer T., Sauer U., Hough D. W. and Danson M. J.
1177   (2010) Metabolism of pentose sugars in the hyperthermophilic archaea Sulfolobus
1178   solfataricus and Sulfolobus acidocaldarius. *Journal of Biological Chemistry* **285**, 33701–
1179   33709.
1180   Oger P. M. and Cario A. (2013) Adaptation of the membrane in Archaea. *Biophysical chemistry*
1181   **183**, 42–56.
1182   Osburn M. R., Dawson K. S., Fogel M. L. and Sessions A. L. (2016) Fractionation of hydrogen
1183   isotopes by sulfate-and nitrate-reducing bacteria. *Frontiers in microbiology* **7**, 1166.
1184   Pearson A. (2019) Resolving a piece of the archaeal lipid puzzle. *Proceedings of the National*
1185   *Academy of Sciences* **116**, 22423–22425.
1186   Pearson A., Hurley S. J., Walter S. R. S., Kusch S., Lichtin S. and Zhang Y. G. (2016) Stable
1187   carbon isotope ratios of intact GDGTs indicate heterogeneous sources to marine
1188   sediments. *Geochimica et Cosmochimica Acta* **181**, 18–35.
1189   Pearson A. and Ingalls A. E. (2013) Assessing the use of archaeal lipids as marine environmental
1190   proxies. *Annual Review of Earth and Planetary Sciences* **41**, 359–384.
1191   Peregrina J. R., Sánchez-Azqueta A., Herguedas B., Martínez-Júlvez M. and Medina M. (2010)
1192   Role of specific residues in coenzyme binding, charge–transfer complex formation, and
1193   catalysis in Anabaena ferredoxin NADP+-reductase. *Biochimica et Biophysica Acta*
1194   *(BBA) - Bioenergetics* **1797**, 1638–1646.
1195   Polik C. A., Elling F. J. and Pearson A. (2018) Impacts of paleoecology on the TEX86 sea
1196   surface temperature proxy in the Pliocene-Pleistocene Mediterranean Sea.
1197   *Paleoceanography and Paleoclimatology* **33**, 1472–1489.
1198   Poudel S., Dunham E. C., Lindsay M. R., Amenabar M. J., Fones E. M., Colman D. R. and Boyd
1199   E. S. (2018) Origin and evolution of flavin-based electron bifurcating enzymes. *Frontiers*
1200   *in microbiology* **9**, 1762.

1201 Powers L., Werne J. P., Vanderwoude A. J., Damsté J. S. S., Hopmans E. C. and Schouten S.
1202   (2010) Applicability and calibration of the TEX86 paleothermometer in lakes. *Organic*
1203   *Geochemistry* **41**, 404–413.
1204 Qin W., Amin S. A., Lundeen R. A., Heal K. R., Martens-Habbena W., Turkarslan S., Urakawa
1205   H., Costa K. C., Hendrickson E. L. and Wang T. (2018) Stress response of a marine
1206   ammonia-oxidizing archaeon informs physiological status of environmental populations.
1207   *The ISME journal* **12**, 508–519.
1208 Qin W., Amin S. A., Martens-Habbena W., Walker C. B., Urakawa H., Devol A. H., Ingalls A.
1209   E., Moffett J. W., Armbrust E. V. and Stahl D. A. (2014) Marine ammonia-oxidizing
1210   archaeal isolates display obligate mixotrophy and wide ecotypic variation. *Proceedings of*
1211   *the National Academy of Sciences* **111**, 12504–12509.
1212 Quehenberger J., Pittenauer E., Allmaier G. and Spadiut O. (2020) The influence of the specific
1213   growth rate on the lipid composition of Sulfolobus acidocaldarius. *Extremophiles* **24**,
1214   413.
1215 Ren M., Feng X., Huang Y., Wang H., Hu Z., Clingenpeel S., Swan B. K., Fonseca M. M.,
1216   Posada D., Stepanauskas R., Hollibaugh J. T., Foster P. G., Woyke T. and Luo H. (2019)
1217   Phylogenomics suggests oxygen availability as a driving force in Thaumarchaeota
1218   evolution. *The ISME Journal* **13**, 2150–2161.
1219 Robert F. (2001) The Origin of Water on Earth. *Science* **293**, 1056.
1220 Sachs J. P. (2014) Hydrogen Isotope Signatures in the Lipids of Phytoplankton. In *Treatise on*
1221   *Geochemistry* Elsevier. pp. 79–94.
1222 Sachs J. P. and Kawka O. E. (2015) The influence of growth rate on 2H/1H fractionation in
1223   continuous cultures of the coccolithophorid Emiliania huxleyi and the diatom
1224   Thalassiosira pseudonana. *Plos one* **10**, e0141643.
1225 Sachs J. P., Maloney A. E. and Gregersen J. (2017) Effect of light on 2H/1H fractionation in
1226   lipids from continuous cultures of the diatom Thalassiosira pseudonana. *Geochimica et*
1227   *Cosmochimica Acta* **209**, 204–215.
1228 Sachs J. P., Maloney A. E., Gregersen J. and Paschall C. (2016) Effect of salinity on 2H/1H
1229   fractionation in lipids from continuous cultures of the coccolithophorid Emiliania
1230   huxleyi. *Geochimica et Cosmochimica Acta* **189**, 96–109.
1231 Sachse D., Billault I., Bowen G. J., Chikaraishi Y., Dawson T. E., Feakins S. J., Freeman K. H.,
1232   Magill C. R., McInerney F. A. and Van Der Meer M. T. (2012) Molecular
1233   paleohydrology: interpreting the hydrogen-isotopic composition of lipid biomarkers from
1234   photosynthesizing organisms. *Annual Review of Earth and Planetary Sciences* **40**, 221–
1235   249.
1236 Sachse D., Gleixner G., Wilkes H. and Kahmen A. (2010) Leaf wax n-alkane δD values of field-
1237   grown barley reflect leaf water δD values at the time of leaf formation. *Geochimica et*
1238   *Cosmochimica Acta* **74**, 6741–6750.
1239 Sánchez-Azqueta A., Herguedas B., Hurtado-Guerrero R., Hervás M., Navarro J. A., Martínez-
1240   Júlvez M. and Medina M. (2014) A hydrogen bond network in the active site of
1241   Anabaena ferredoxin-NADP+ reductase modulates its catalytic efficiency. *Biochimica et*
1242   *Biophysica Acta (BBA) - Bioenergetics* **1837**, 251–263.
1243 Santoro A. E. and Casciotti K. L. (2011) Enrichment and characterization of ammonia-oxidizing
1244   archaea from the open ocean: phylogeny, physiology and stable isotope fractionation. *The*
1245   *ISME journal* **5**, 1796–1808.

1246 Sasaki D., Fujihashi M., Iwata Y., Murakami M., Yoshimura T., Hemmi H. and Miki K. (2011)
1247   Structure and Mutation Analysis of Archaeal Geranylgeranyl Reductase. *Journal of*
1248   *Molecular Biology* **409**, 543–557.
1249 Sato S., Murakami M., Yoshimura T. and Hemmi H. (2008) Specific Partial Reduction of
1250   Geranylgeranyl Diphosphate by an Enzyme from the Thermoacidophilic Archaeon
1251   *Sulfolobus acidocaldarius* Yields a Reactive Prenyl Donor, Not a Dead-End Product. *J*
1252   *Bacteriol* **190**, 3923–3929.
1253 Sauer U., Canonaco F., Heri S., Perrenoud A. and Fischer E. (2004) The soluble and membrane-
1254   bound transhydrogenases UdhA and PntAB have divergent functions in NADPH
1255   metabolism of Escherichia coli. *Journal of Biological Chemistry* **279**, 6613–6619.
1256 Schimmelmann A., Sessions A. L. and Mastalerz M. (2006) Hydrogen isotopic (D/H)
1257   composition of organic matter during diagenesis and thermal maturation. *Annu. Rev.*
1258   *Earth Planet. Sci.* **34**, 501–533.
1259 Schouten S., Hopmans E. C. and Damsté J. S. S. (2013) The organic geochemistry of glycerol
1260   dialkyl glycerol tetraether lipids: A review. *Organic geochemistry* **54**, 19–61.
1261 Schouten S., Hopmans E. C., Schefuß E. and Damste J. S. S. (2002) Distributional variations in
1262   marine crenarchaeotal membrane lipids: a new tool for reconstructing ancient sea water
1263   temperatures? *Earth and Planetary Science Letters* **204**, 265–274.
1264 Schouten S., Ossebaar J., Schreiber K., Kienhuis M., Langer G., Benthien A. and Bijma J. (2006)
1265   The effect of temperature, salinity and growth rate on the stable hydrogen isotopic
1266   composition of long chain alkenones produced by Emiliania huxleyi and Gephyrocapsa
1267   oceanica. *Biogeosciences* **3**, 113–119.
1268 Sessions A. L. (2016) Factors controlling the deuterium contents of sedimentary hydrocarbons.
1269   *Organic Geochemistry* **96**, 43–64.
1270 Sessions A. L., Burgoyne T. W., Schimmelmann A. and Hayes J. M. (1999) Fractionation of
1271   hydrogen isotopes in lipid biosynthesis. *Organic Geochemistry* **30**, 1193–1200.
1272 Sessions A. L., Jahnke L. L., Schimmelmann A. and Hayes J. M. (2002) Hydrogen isotope
1273   fractionation in lipids of the methane-oxidizing bacterium Methylococcus capsulatus.
1274   *Geochimica et Cosmochimica Acta* **66**, 3955–3969.
1275 Sessions A. L., Sylva S. P., Summons R. E. and Hayes J. M. (2004) Isotopic exchange of carbon-
1276   bound hydrogen over geologic timescales. *Geochimica et Cosmochimica Acta* **68**, 1545–
1277   1559.
1278 Shafiee R. T., Snow J. T., Hester S., Zhang Q. and Rickaby R. E. (2022) Proteomic response of
1279   the marine ammonia-oxidising archaeon Nitrosopumilus maritimus to iron limitation
1280   reveals strategies to compensate for nutrient scarcity. *Environmental Microbiology* **24**,
1281   835–849.
1282 Shah S. R., Mollenhauer G., Ohkouchi N., Eglinton T. I. and Pearson A. (2008) Origins of
1283   archaeal tetraether lipids in sediments: Insights from radiocarbon analysis. *Geochimica et*
1284   *Cosmochimica Acta* **72**, 4577–4594.
1285 Sinninghe Damsté J., Pancost R. and Hopmans E. (2001) Archaeal lipids in Mediterranean Cold
1286   Seeps: Molecular proxies for anaerobic methane oxidation. *Geochimica et Cosmochimica*
1287   *Acta* **65**, 1611.
1288 Sinninghe Damsté J. S., Weber Y., Zopfi J., Lehmann M. F. and Niemann H. (2022)
1289   Distributions and sources of isoprenoidal GDGTs in Lake Lugano and other central
1290   European (peri-)alpine lakes: Lessons for their use as paleotemperature proxies.
1291   *Quaternary Science Reviews* **277**, 107352.

1292   Smith F. A. and Freeman K. H. (2006) Influence of physiology and climate on δD of leaf wax n-
1293   alkanes from C3 and C4 grasses. *Geochimica et Cosmochimica Acta* **70**, 1172–1187.
1294   Spaans S. K., Weusthuis R. A., Van Der Oost J. and Kengen S. W. (2015) NADPH-generating
1295   systems in bacteria and archaea. *Frontiers in microbiology* **6**, 742.
1296   Taenzer L., Labidi J., Masterson A. L., Feng X., Rumble III D., Young E. D. and Leavitt W. D.
1297   (2020) Low Δ12CH2D2 values in microbialgenic methane result from combinatorial
1298   isotope effects. *Geochimica et Cosmochimica Acta* **285**, 225–236.
1299   Taylor K. W., Huber M., Hollis C. J., Hernandez-Sanchez M. T. and Pancost R. D. (2013) Re-
1300   evaluating modern and Palaeogene GDGT distributions: Implications for SST
1301   reconstructions. *Global and Planetary Change* **108**, 158–174.
1302   Tierney J. E. and Tingley M. P. (2014) A Bayesian, spatially-varying calibration model for the
1303   TEX86 proxy. *Geochimica et Cosmochimica Acta* **127**, 83–106.
1304   Tierney J. E. and Tingley M. P. (2015) A TEX 86 surface sediment database and extended
1305   Bayesian calibration. *Scientific data* **2**, 1–10.
1306   Tipple B. J., Berke M. A., Doman C. E., Khachaturyan S. and Ehleringer J. R. (2013) Leaf-wax
1307   n-alkanes record the plant–water environment at leaf flush. *Proceedings of the National
1308   Academy of Sciences* **110**, 2659–2664.
1309   Tourte M., Schaeffer P., Grossi V. and Oger P. M. (2022) Membrane adaptation in the
1310   hyperthermophilic archaeon Pyrococcus furiosus relies upon a novel strategy involving
1311   glycerol monoalkyl glycerol tetraether lipids. *Environmental Microbiology* **24**, 2029–
1312   2046.
1313   Valentine D. L. (2007) Adaptations to energy stress dictate the ecology and evolution of the
1314   Archaea. *Nature Reviews Microbiology* **5**, 316–323.
1315   Valentine D., Sessions A., Tyler S. and Chidthaisong A. (2004) Hydrogen isotope fractionation
1316   during H2/CO2 acetogenesis: hydrogen utilization efficiency and the origin of lipid-
1317   bound hydrogen. *Geobiology* **2**, 179–188.
1318   Wakeham S. G., Lewis C. M., Hopmans E. C., Schouten S. and Damsté J. S. S. (2003) Archaea
1319   mediate anaerobic oxidation of methane in deep euxinic waters of the Black Sea.
1320   *Geochimica et Cosmochimica Acta* **67**, 1359–1374.
1321   Walker C. B., De La Torre J., Klotz M., Urakawa H., Pinel N., Arp D., Brochier-Armanet C.,
1322   Chain P., Chan P. and Gollabgir A. (2010) Nitrosopumilus maritimus genome reveals
1323   unique mechanisms for nitrification and autotrophy in globally distributed marine
1324   crenarchea. *Proceedings of the National Academy of Sciences* **107**, 8818–8823.
1325   Wang Y., Sessions A. L., Nielsen R. J. and Goddard III W. A. (2009) Equilibrium 2H/1H
1326   fractionations in organic molecules: I. Experimental calibration of ab initio calculations.
1327   *Geochimica et Cosmochimica Acta* **73**, 7060–7075.
1328   Wegener G., Kellermann M. Y. and Elvert M. (2016) Tracking activity and function of
1329   microorganisms by stable isotope probing of membrane lipids. *Current Opinion in
1330   Biotechnology* **41**, 43–52.
1331   Weijers J. W., Schouten S., Schefuß E., Schneider R. R. and Damste J. S. S. (2009)
1332   Disentangling marine, soil and plant organic carbon contributions to continental margin
1333   sediments: a multi-proxy approach in a 20,000 year sediment record from the Congo
1334   deep-sea fan. *Geochimica et Cosmochimica Acta* **73**, 119–132.
1335   Wijker R. S., Sessions A. L., Fuhrer T. and Phan M. (2019) 2H/1H variation in microbial lipids
1336   is controlled by NADPH metabolism. *Proceedings of the National Academy of Sciences*
1337   **116**, 12173–12182.

1338   Wolfshorndl M., Danford R. and Sachs J. P. (2019) 2H/1H fractionation in microalgal lipids
1339   from the North Pacific Ocean: Growth rate and irradiance effects. *Geochimica et*
1340   *Cosmochimica Acta* **246**, 317–338.
1341   Wu W., Meador T. B., Könneke M., Elvert M., Wegener G. and Hinrichs K. (2020) Substrate-
1342   dependent incorporation of carbon and hydrogen for lipid biosynthesis by
1343   Methanosarcina barkeri. *Environmental Microbiology Reports* **12**, 555–567.
1344   Zeng Z., Chen H., Yang H., Chen Y., Yang W., Feng X., Pei H. and Welander P. V. (2022)
1345   Identification of a protein responsible for the synthesis of archaeal membrane-spanning
1346   GDGT lipids. *Nature Communications* **13**, 1545.
1347   Zeng Z., Liu X.-L., Farley K. R., Wei J. H., Metcalf W. W., Summons R. E. and Welander P. V.
1348   (2019) GDGT cyclization proteins identify the dominant archaeal sources of tetraether
1349   lipids in the ocean. *Proc Natl Acad Sci USA*, 201909306.
1350   Zhang X., Gillespie A. L. and Sessions A. L. (2009) Large D/H variations in bacterial lipids
1351   reflect central metabolic pathways. *Proceedings of the National Academy of Sciences*
1352   **106**, 12580–12586.
1353   Zhang Y. G., Pagani M. and Wang Z. (2016) Ring Index: A new strategy to evaluate the integrity
1354   of TEX86 paleothermometry. *Paleoceanography* **31**, 220–232.
1355   Zhang Y. G., Zhang C. L., Liu X.-L., Li L., Hinrichs K.-U. and Noakes J. E. (2011) Methane
1356   Index: A tetraether archaeal lipid biomarker indicator for detecting the instability of
1357   marine gas hydrates. *Earth and Planetary Science Letters* **307**, 525–534.
1358   Zhou A., Weber Y., Chiu B. K., Elling F. J., Cobban A. B., Pearson A. and Leavitt W. D. (2020)
1359   Energy flux controls tetraether lipid cyclization in Sulfolobus acidocaldarius.
1360   *Environmental microbiology* **22**, 343–353.
1361
1362
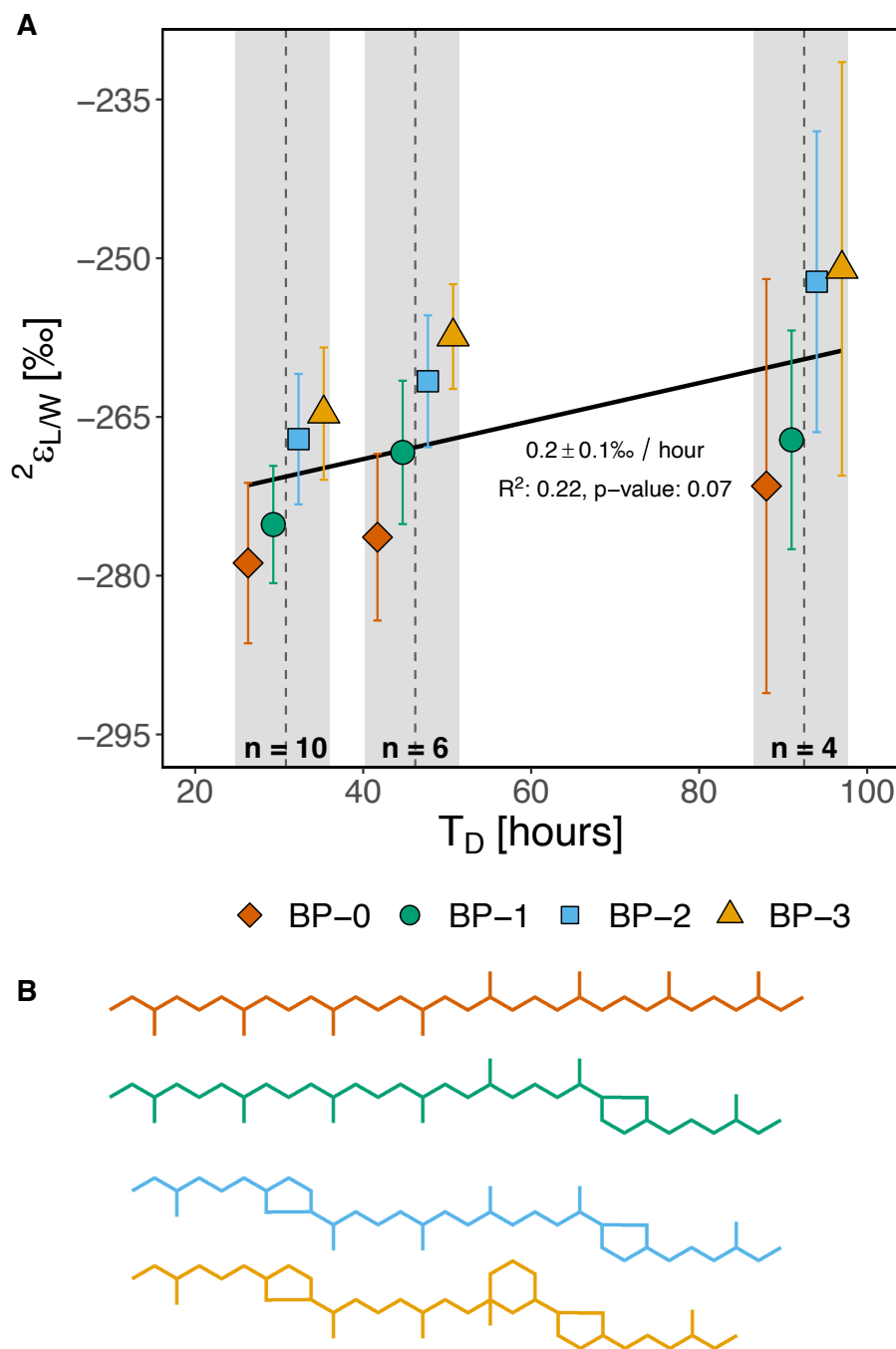
Figure 1:

Figure 1. (**A**) The hydrogen isotope fractionation ($^2\varepsilon_{L/W}$) between growth medium water and biphytanes (BPs) in response to doubling time (T_D) for *N. maritimus* cultivated at 28 °C and pH 7.5-7.6. Black line shows the slope (‰ / hour) for abundance-weighted linear regression of all biphytane $^2\varepsilon_{L/W}$ values vs. T_D. (**B**) Structures of the BPs (color-coded to match data shown in A).
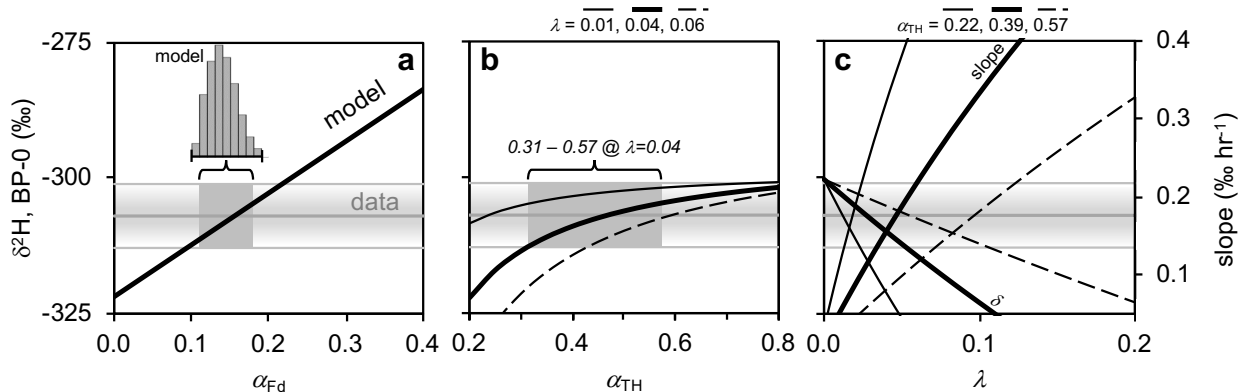
Figure 2:
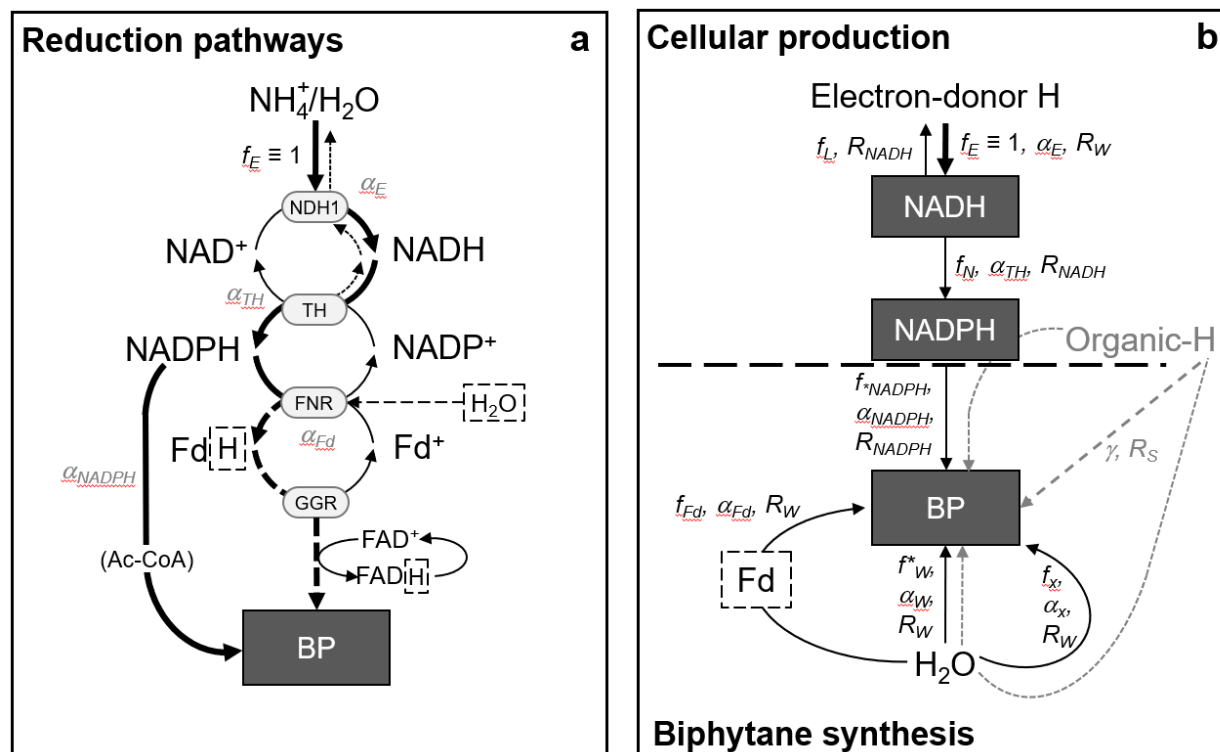
Figure 2. (a) Sources of biosynthetic H for biphytane (BP) synthesis in *N. maritimus*. Respiratory complex 1 (NDH1) and an unknown transhydrogenase (TH) transfer H to NADPH. This NADPH either is a direct source of anabolic H to BPs (via Ac-CoA and further reactions; see Figure 3) or the e^- are transferred to ferredoxin-NAD$^+$ reductase (FNR, which takes H$^+$ from H$_2$O). FNR is the suggested donor for geranylgeranyl reductase (GGR), which uses FADH as a cofactor. See main text for further details. (b) The resulting isotope flux balance model with simplified sources of H. Cellular production sums above the horizontal dashed line, whereas biphytane sums below. f_i = fractional fluxes; a_i = ^{2}H/^{1}H kinetic isotope effects; R_i = ^{2}H/^{1}H isotope ratios; concept according to Wijker et al., 2019. The Cellular production module controls the isotope balance of NADPH, which flows into the Biphytane synthesis module. Thus, f_N and $f_{*\mathrm{NADPH}}$ are not equal; f_N is a fraction of total available reducing power, f_E (with the remainder leaked via the NADH pool, f_L), while $f_{*\mathrm{NADPH}}$ is a fraction of biphytane stoichiometric flux. Processes that would incorporate H from acetate and organic substrates are shown in grey: thin dashed arrows signify the partitioning of *de novo* (autotrophic) acetate H into the NADPH and H$_2$O pools, while the fraction (g) of acetate methyl groups that is inherited directly from organic substrates is shown with a long-dashed arrow; in *N. maritimus*, g is always zero. Details about the specific stoichiometry for each BP are shown in Figure 3 and Tables 2, 3, and S2.
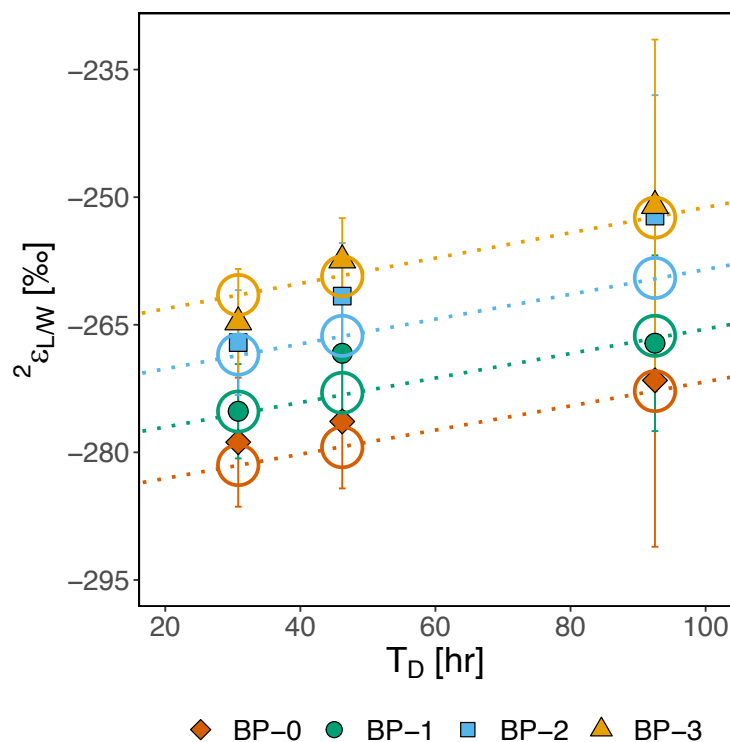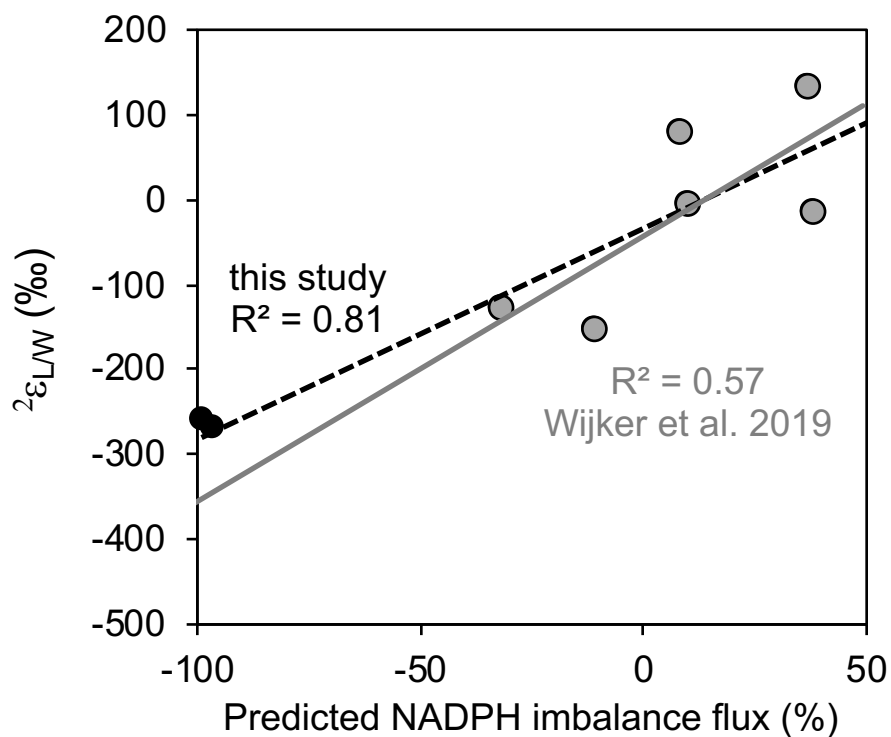
Figure 3:
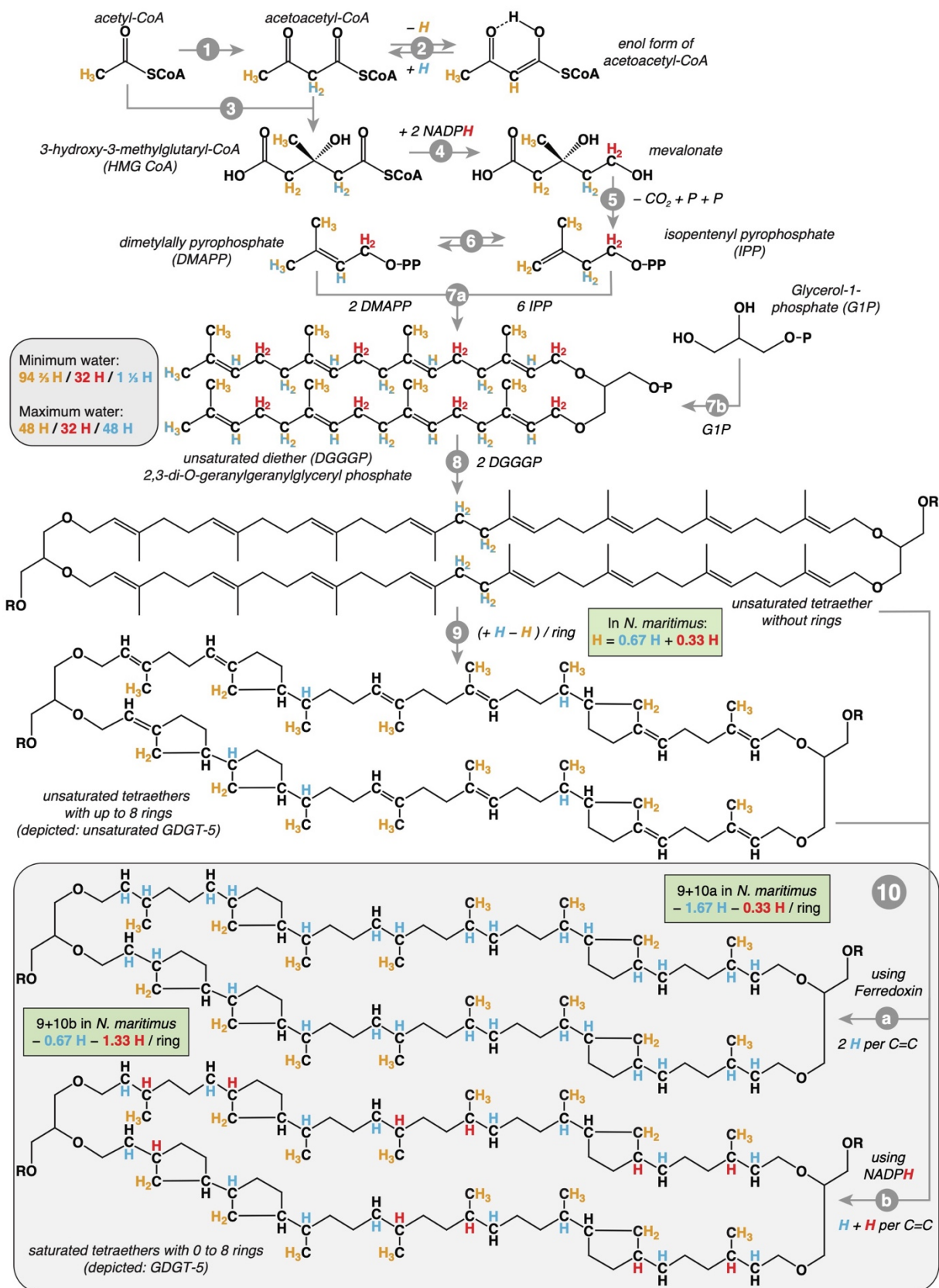
Figure 3. Overview of H sources for archaeal tetraether biosynthesis. Here (orange) H from acetyl-CoA; (red) H from NADPH; (blue) H from protons (water-derived H^+). Mixed potential sources of H from acetyl-CoA and water are shown half orange/half blue. For clarity, the H that enters lipid synthesis from acetyl-CoA methyl groups is visualized in orange; the biosynthetic sources of this H in *N. maritimus* are shown in Figure S4. The summary box for DGGGP indicates the minimum and maximum numbers of alkyl chain H that could originate from water during tetraether biosynthesis, which depends on the extent of re-equilibration during isomerization steps (2 & 6). See Tables 2, 3, and Table S2 for full accounting of the different scenarios. The net effect of ring formation on H sources combines the formation of the rings (step 9) with correspondingly fewer double bond reductions (step 10). The overall stoichiometry per ring for *N. maritimus* is a net of -1.67 H from water and -0.33 H from NADPH if the GGR pathway is reduction with Ferredoxin (steps 9 + 10a) or -0.67 H from water and -1.33 H from NADPH if NADPH is the cofactor (steps 9 + 10b). See the main text for further discussion. Biosynthetic steps are indicated in grey. 1: acetyl-CoA acetyl transferase; 2: tautomerization of acetoacetyl-CoA (can exchange the H at the C_2 position). 3: HMG CoA synthase; 4: HMG CoA reductase; 5: several alternative pathways from mevalonate to IPP (no H differences); 6: IPP isomerase (can exchange the H at the C_4 position); 7a: geranylgeranyl pyrophosphate synthase; 7b: geranylgeranyl glyceryl phosphate synthase; 8: tetraether synthase (Tes); 9: ring synthases (GrsAB); 10: geranylgeranyl reductase (GGR) using ferredoxin (a) or NADH/NADPH (b) as reductant.

Figure 4:

Figure 4. Sensitivity analysis. The Sensitivity of R_{BP} to model results; Scenario 2, $f_x = 0$, $f_{Fd} \neq 0$. Horizontal grey lines and shaded regions ("data") represent the mean and $\pm 1\sigma$ range for δ^2H values of BP-0 at average T_D. Black lines indicate model results, with dark grey boxes indicating where the model is compatible with the data. The inset histogram in (**a**) shows the frequency distribution of best-fit values of α_{Fd} (mean fit, 0.14 ± 0.02) for Scenario 2, Case A; this version yields $\alpha_E \cdot \alpha_{NADPH} = 0.669$ (Figure S6), *i.e.*, it does not prescribe a value for α_{NADPH}. Scenario 2, Case B yields exact values of $\alpha_{Fd} = 0.132$ and $\alpha_E = 0.743$ when α_{NADPH} is fixed at 0.9; see Table 4 and main text. (**b**) The strong co-dependence of α_{TH} and λ (Figure S6) indicates the minimum likely value of α_{TH} is > the 0.22 boundary value (from PntAB), and that the data would be compatible with values of $\alpha_{TH} > 0.57$ (from sTH) only if λ is > 0.6. (**c**) The predicted growth rate sensitivity (slope, ‰ hr^{-1}), and isotope ratio (negative-slope curves; δ^2H, ‰), are strongly dependent on λ. At the consensus $\alpha_{TH} = 0.39$ (thick lines), the permitted range of λ to satisfy values of δ^2H is ~0.01 – 0.06 (downward sloping thick black line). However, the growth rate sensitivity narrows this range to 0.03-0.05 (upward sloping thick black line). The consensus λ value using $\alpha_{TH} = 0.39$ and data for all compounds is $\lambda = 0.04$ (Table 4).

Figure 5:

Figure 5. Model/data comparison. The $^2\varepsilon_{L/W}$ values for BPs of *N. maritimus* from models and measurements, showing growth-rate and ring-number dependence. Open symbols are the model simulation while closed symbols are the data; calculations use the consensus estimates of kinetic isotope effects for "Scenario 2", Table 4. The growth-rate effect, or slope of $^2\varepsilon_{L/W}$, is modeled to be 0.15 ‰ hr^{-1} (the data yield 0.2 ± 0.1 ‰ hr^{-1}; Figure 1). The ring-dependent enrichment of ^{2}H is modeled to be 6.7 ‰ ring^{-1} (the data yield 6.4 ± 2.7 ‰ ring^{-1}).

Figure 6:

Figure 6. NADPH flux imbalance. Values for or *N. maritimus* agree with the linear dependence of bacterial $^2\varepsilon_{L/W}$ on relative NADPH availability (Wijker et al., 2019). In cells under extreme NADPH deficit, the minimum $^2\varepsilon_{L/W}$ value is predicted to be -282‰ (intercept of all data). This value not only indicates a consistent overall KIE for H cycling within cellular biosynthetic processes, it also agrees with the premise that archaea metabolize under conditions of extreme energy limitation (Valentine, 2007). Original Wijker et al. (2019) data and linear fit are shown in grey and solid line; our data and the new fit are in black and dashed line.

Main Tables 1 - 4

Table 1: Data for individual biphytanes per chemostat rate.

T_D (hr)	#	water δ^2H (‰)	BP-0 (‰) δ^2H	$^2\varepsilon_{L/W}$	BP-1 (‰) δ^2H	$^2\varepsilon_{L/W}$	$\Delta\varepsilon$/ring	BP-2 (‰) δ^2H	$^2\varepsilon_{L/W}$	$\Delta\varepsilon$/ring	BP-3 (‰) δ^2H	$^2\varepsilon_{L/W}$	$\Delta\varepsilon$/ring	relative abundance (%) BP-0	BP-1	BP-2	BP-3	weighted avg. $^2\varepsilon_{L/W}$ (‰)
30.8	10	-44.0	-311 ± 7	-279 ± 8	-307 ± 5	-275 ± 6	3.6	-299 ± 6	-267 ± 6	7.0	-297 ± 6	-265 ± 6	4.1	27 ± 1	31 ± 1	25 ± 1	17 ± 1	-272 ± 6
46.2	6	-42.0	-307 ± 8	-276 ± 8	-299 ± 6	-268 ± 7	8.0	-293 ± 6	-262 ± 6	7.0	-289 ± 5	-257 ± 5	5.3	22 ± 1	24 ± 1	32 ± 1	22 ± 1	-266 ± 7
92.5	4	-44.0	-304 ± 19	-272 ± 20	-299 ± 10	-267 ± 10	4.4	-285 ± 14	-252 ± 14	12.3	-284 ± 19	-251 ± 20	5.4	17 ± 1	32 ± 1	29 ± 1	21 ± 1	-260 ± 8

	$^2\varepsilon_{L/W}$	$\Delta^2\varepsilon$/ring
Average (all BPs)	-266 ± 9 ‰	6.4 ± 2.7 ‰

* Data and processing scripts for GC-P-IRMS output are available at: https://github.com/KopfLab/2022_leavitt_et_al.

Table 2: Stoichiometric summary of hydrogen sources to archaeal BP-0. Detailed stoichiometry in Table S1.

Biosynthetic Scenarios	BP-0 ($C_{40}H_{80}$) Ac-CoA	H_2O	NAD(P)H	Fd (H⁻)	H_2O-Exch
	f_A	f_{GGR_W} $f_{LipSynth\_W}$	f_{GGR_NADPH} $f_{LipSynth\_NADPH}$	f_{GGR_Fd}	f_x
Scenario 1:	47 ⅓	8 ⅔	8 16	0	0
Scenario 2:	47 ⅓	8 ⅔	0 16	8	0
Scenario 3:	24	8 0	8 16	0	24
Scenario 4:	24	8 0	0 16	8	24

Table 3: Changes in biosynthetic H source for ring-containing biphytanes relative to BP-0 for organisms producing Ac-CoA autotrophically via the 3HP/4HB pathway. Details in Table S1.

|		$(f_{*W} + f_x)$	f_{*NADPH}	f_{Fd}
Scenario 1	BP-1	0.43%	-0.43%	--
	BP-2	0.89%	-0.89%	--
	BP-3	1.37%	-1.37%	--
Scenario 2	BP-1	0.43%	0.59%	-1.03%
	BP-2	0.89%	1.21%	-2.11%
	BP-3	1.37%	1.87%	-3.24%
Scenario 3	BP-1	0.68%	-0.68%	--
	BP-2	1.40%	-1.40%	--
	BP-3	2.16%	-2.16%	--
Scenario 4	BP-1	0.68%	0.34%	-1.03%
	BP-2	1.40%	0.70%	-2.11%
	BP-3	2.16%	1.08%	-3.24%

Table 4: Model results for KIEs α_W, α_{TH}, α_E, α_{Fd}, and α_{NADPH}, and flux coefficient λ.

Parameter	Scenario 2, Case A	Scenario 2, Case B
α_W	≥ 0.9	set, 0.9
α_{Fd}	0.14 ± 0.02	0.132
α_{NADPH}	product = 0.669	set, 0.9
α_E		0.743
α_{TH}	range, 0.22-0.57[a]	
λ	range, 0.013-0.061	

[a] Minimum and maximum KIE of hypothetical transhydrogenation, set as the limits of soluble and membrane-bound transhydrogenase KIEs reported in Wijker et al., 2019.

Supplemental Figures 1 - 6

Figure S1: All Biphytane H-Isotope Data
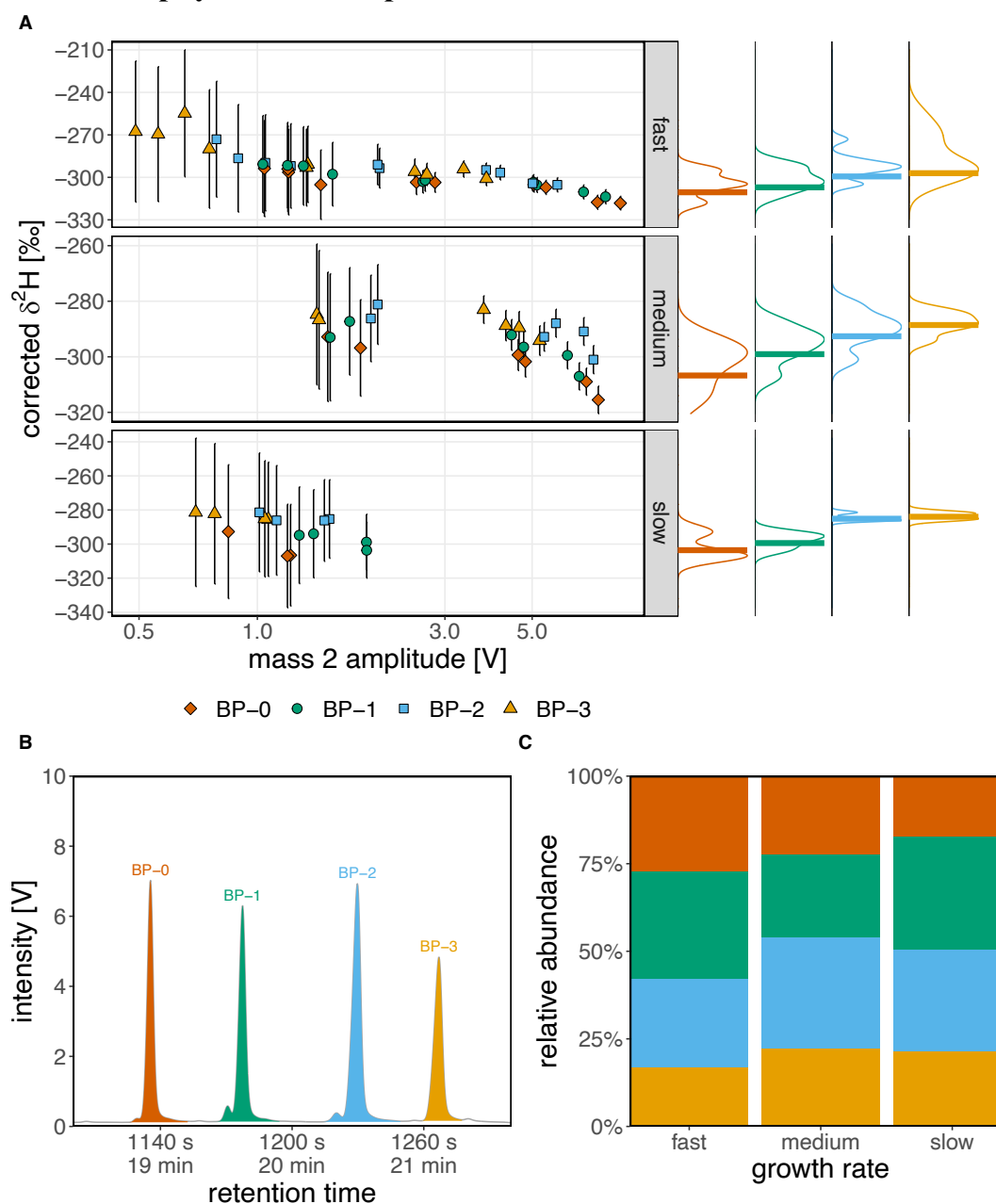
Figure S1. (A) Replicate hydrogen isotope measurements of archaeal biphytanes (BPs) from *N. maritimus*. All isotope values are calibrated against the A6 alkane standard and corrected for alkyl iodide hydrogenation (δ^2H_{cor}) with propagated errors (σ_{cor}) from hydrogenation and peak-size adjusted uncertainties as described in the methods section. **(B)** Example chromatogram showing mass-2 trace of GC-P-IRMS analysis with BPs highlighted. **(C)** Relative abundances of BPs at the "Fast", "Medium", and "Slow" growth rates used in this study (see Table 1 for doubling times).

Figure S2: IRMS Calibration
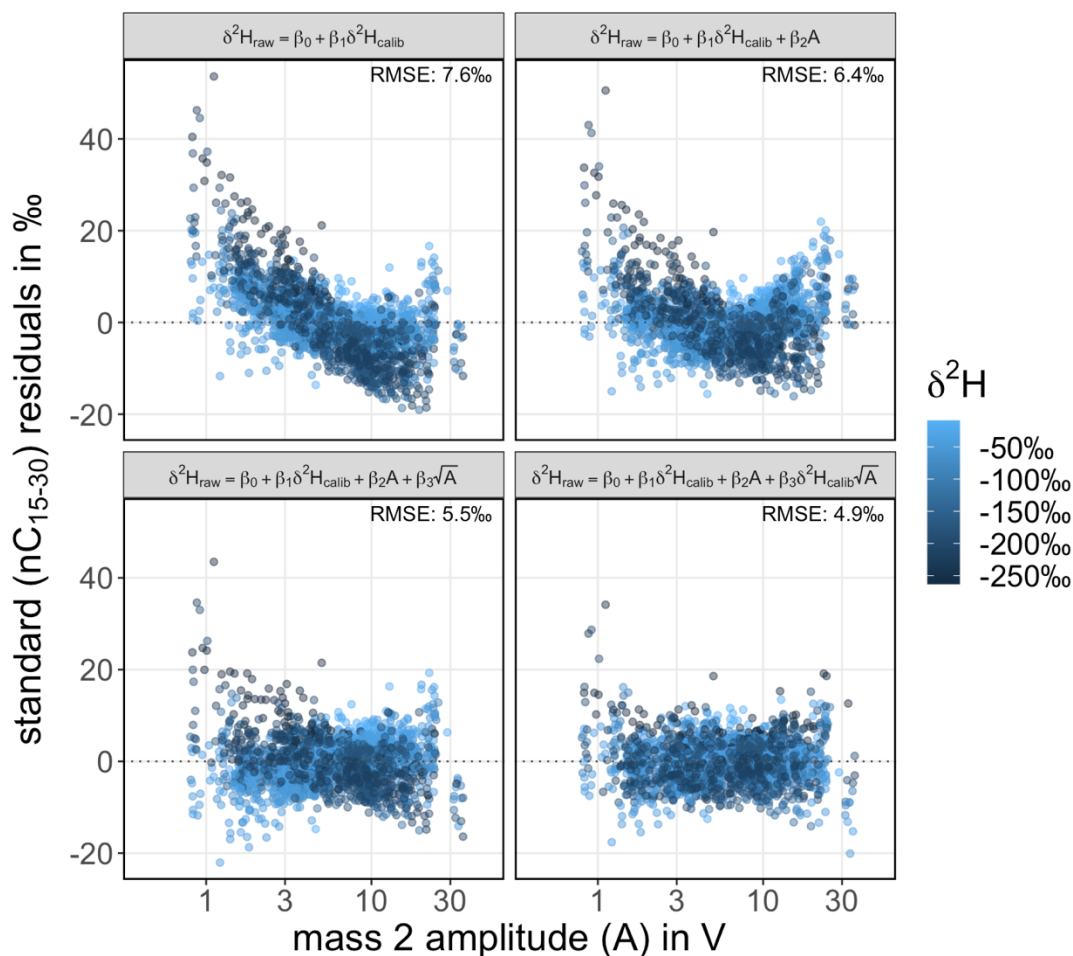
Figure S2. Residuals of the 2195 compound-specific H isotope measurements from the A6 standard compounds (C_{15} through C_{30} n-alkanes) using 4 different multivariate linear calibration models. The regression equation and root-mean-square error (RMSE) of each model are shown in their respective panel. The regression model whose residuals are shown in the lower right panel ($\delta^2\text{H}_{\text{raw}} = \beta_0 + \beta_1 \cdot \delta^2\text{H}_{\text{cal}} + \beta_2 \cdot A + \beta_3 \cdot \delta^2\text{H}_{\text{cal}} \cdot \sqrt{A}$, RMSE 4.9 ‰) is the one used for calibration as discussed in the main text.

Figure S3: H-Isotope Absolute Error Estimates
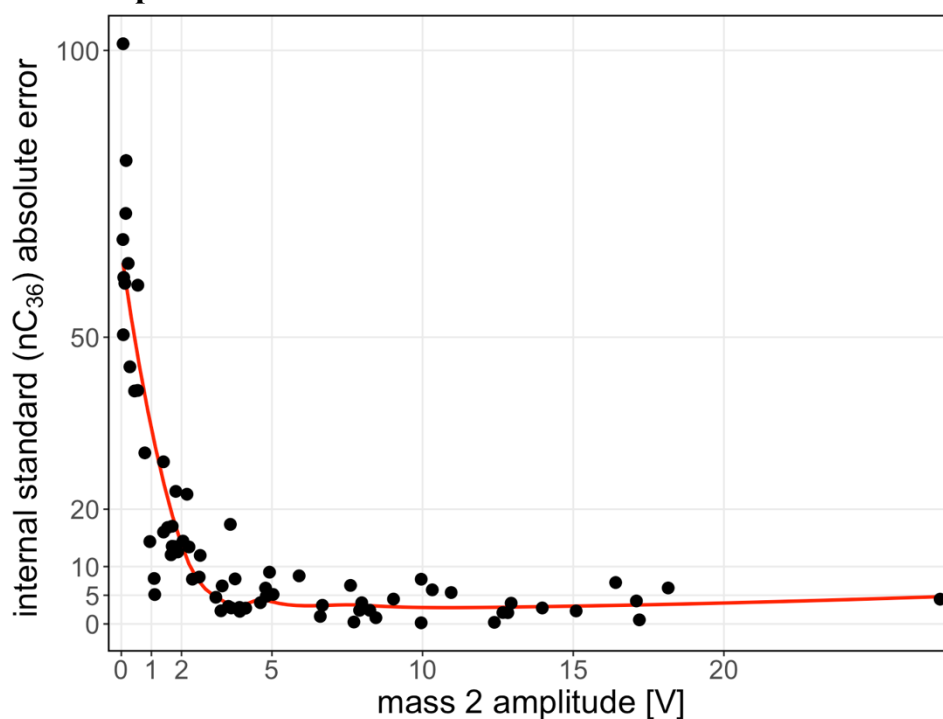
Figure S3. Absolute error of the calibrated δ^2H_{cal} values of the nC_{36} standard (n=73) vs its known isotopic composition. The red line represents a local polynomial regression fit and was used to determine peak-sized adjusted error estimates for the δ^2H_{cal} values (σ_{cal}) of the measured biphytanes (Figures 1 and S1).

Figure S4: 3HP/4HP
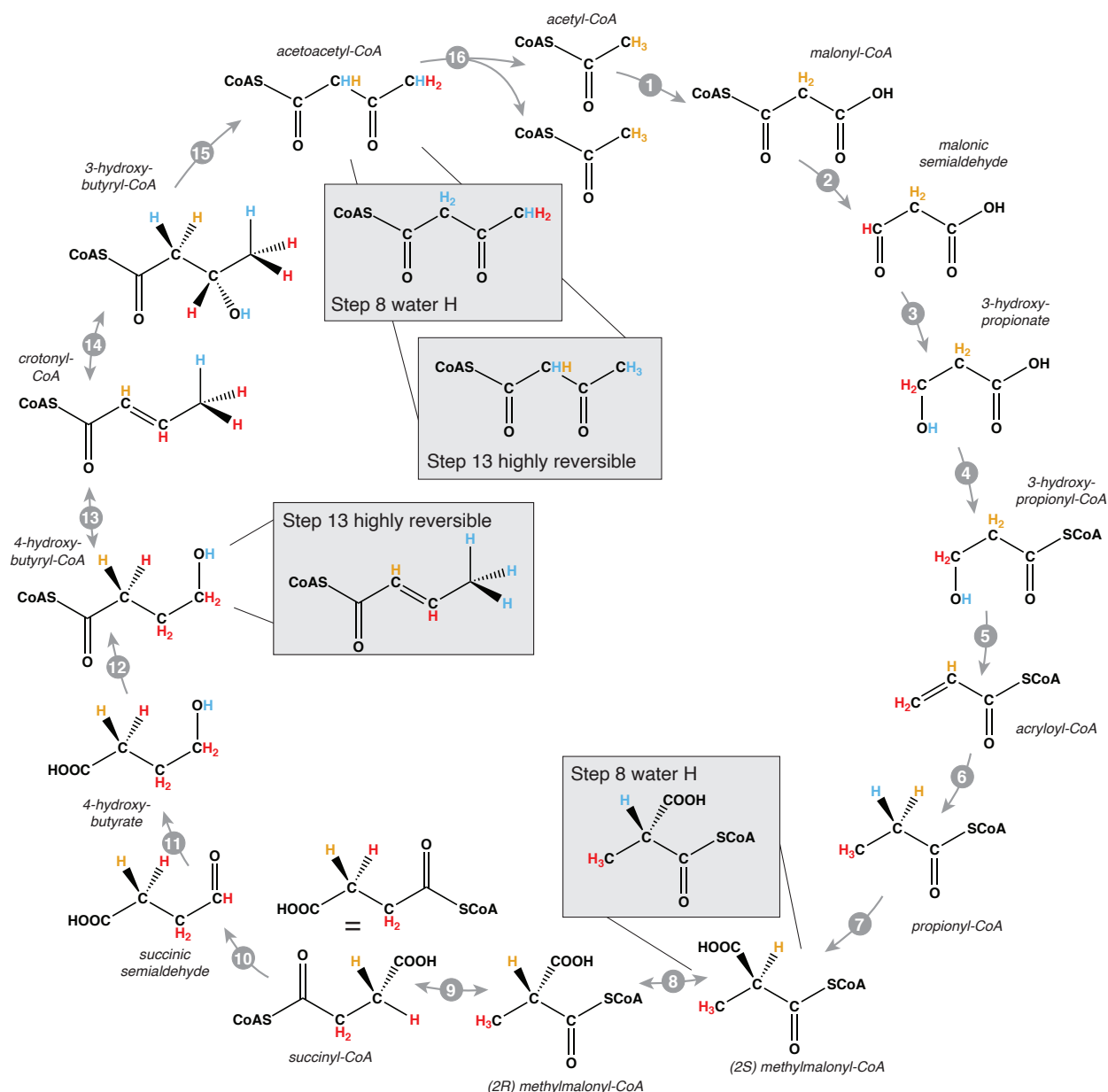
Figure S4. Origin of the methyl group hydrogens of acetyl-CoA derived from the 3HP/4HP (3-hydroxyproprionate / 4-hydroxybutyrate) cycle. The H from water (protons) are shown in blue; H from NADPH in red. One full turn of the cycle generates newly biosynthesized acetyl-CoA (orange) in which all H were originally derived from water and NADPH; all, or all but one, of these H are replaced by the next turn of the cycle. The color coding shows H sources for the maximum efficiency and stereospecificity of all enzymes: the resulting acetoacetyl-CoA incorporates 60% H from water and 40% H from NADPH (maximum possible from NADPH). Methylmalonyl-CoA epimerase (step 8) has a high likelihood of introducing water H at the α-C ("Step 8 water H") (WÖLFLE *et al.*, 1986), thus removing the H from the original acetyl CoA: the resulting acetyl-CoA incorporates 2/3 (66.67%) H from water and 1/3 (33.33%) H from

NADPH. If 4-hydroybutyryl-CoA dehydratase (step 13) is highly reversible under physiological conditions, the 2 H at the ω-C also can be fully exchanged with H from water (Friedrich *et al.*, 2008): the resulting acetyl-CoA ("Step 13 highly reversible") would then incorporate 100% water-H and 0% from NADPH. We consider water introduction at step 8 highly likely, but preserve the original H at step 13, and thus base the modelling discussed in the main text on this scenario. Enzymatic steps are indicated with grey arrows. 1: Acetyl-CoA carboxylase, 2: Malonyl CoA reductase, 3: Malonic semialdehyde reductase, 4: 3-hydroxypropionyl-CoA synthetase, 5: 3-hydroxypropionyl-CoA dehydratase, 6: Acryloyl-CoA reductase, 7: Propionyl-CoA carboxylase, 8: Methylmalonyl CoA epimerase, 9: Methylmalonyl-CoA mutase, 10: Succinyl-CoA reductase, 11: Succinic semialdehyde reductase, 12: 4-Hydroxybutyryl-CoA synthetase, 13: 4-Hydroxybutyryl-CoA dehydratase, 14: Crotonyl-CoA hydratase, 15: 3-Hydroxybutyryl-CoA dehydrogenase, 16: Acetoacetyl-CoA β-ketothiolase. Most carboxylic acids are partly deprotonated at physiological pH but are shown fully protonated for simplicity.

Figure S5: Stoichiometric Fluxes
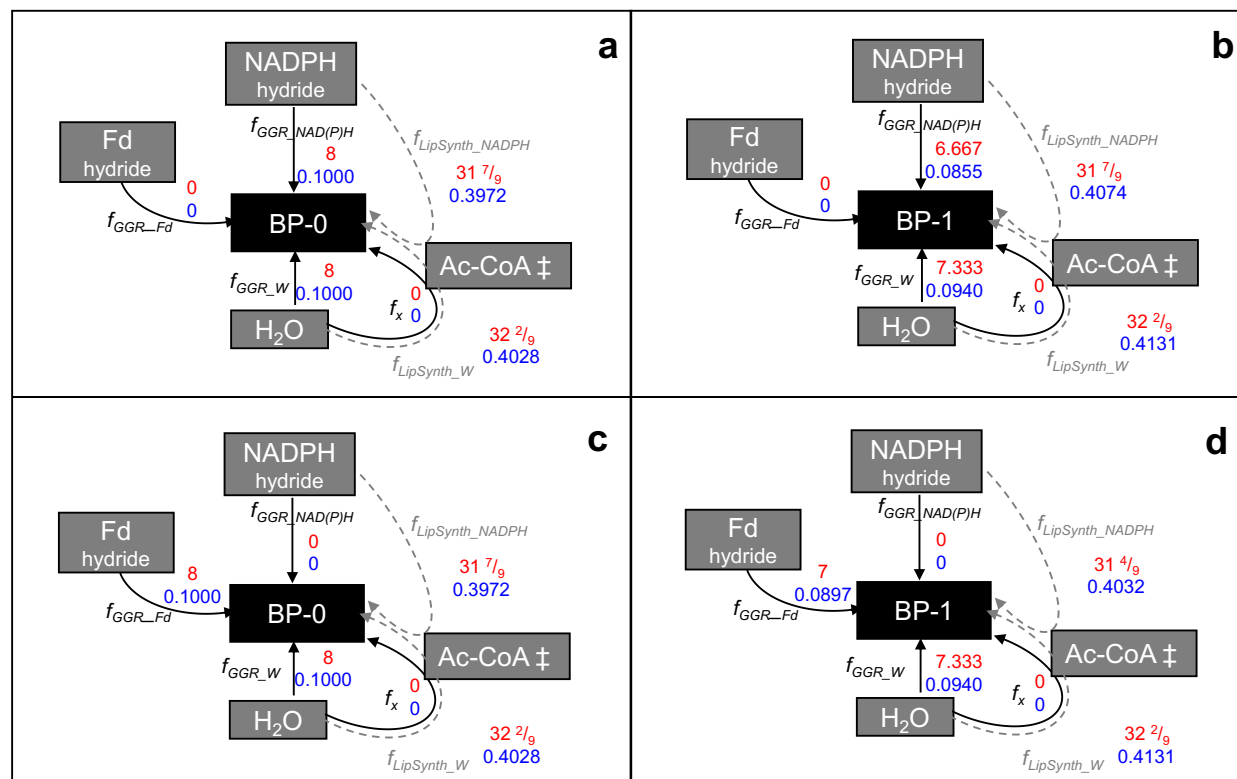
Figure S5. Details of the stoichiometric fluxes of anabolic hydrogen for archaeal lipid biosynthesis (see Figure 2 for schematic overview), showing absolute (red) and relative (blue) stoichiometry for BP-0 (**a**, **c**) and BP-1 (**b**, **d**); other BPs beyond BP-1 change proportionally (Table 3, Table S2). The two potential hydride sources for geranylgeranyl reductase (GGR) are NAD(P)H (**a**, **b**) and ferredoxin (Fd; **c**, **d**), with the paired proton derived in each case from water (f_{GGR_W}). The other protons that form the BP polyprene chains are inherited from Ac-CoA and gained from NADPH during synthesis of IPP; one additional proton from water enters via DMAPP/IPP isomerization (Figure 2, step 6), resulting in the usual fractional distribution between $f_{LipSynth\_W}$ and $f_{LipSynth\_NADPH}$. Ac-CoA also is permitted in some modeled scenarios to exchange protons with water during keto/enol tautomerization (Figure 2, step 2; f_x) although in the four examples shown here this value is set to zero.

Figure S6: Model Dependencies
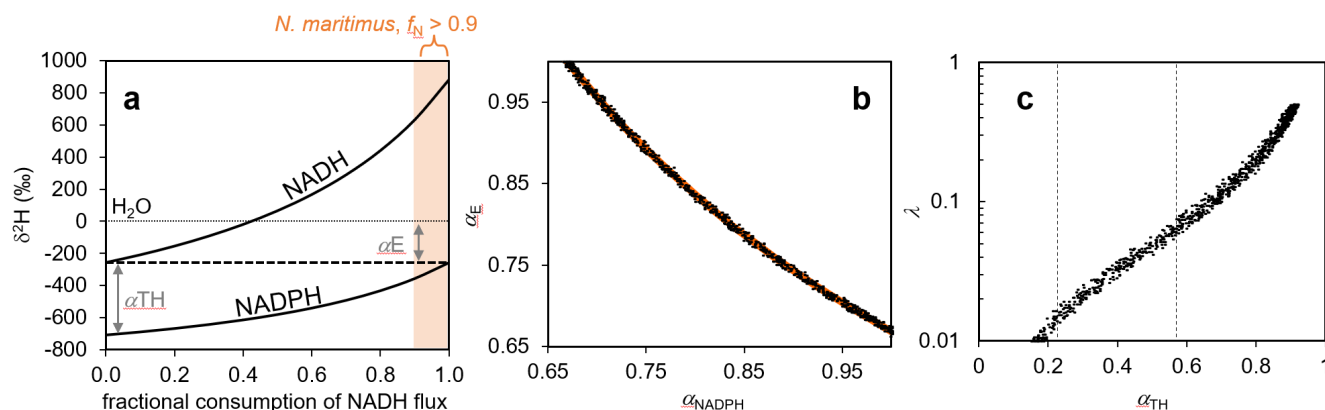
Figure S6. (**a**) Co-dependence of δ^2H of the NADH and NADPH pools generated by Cellular production (Figure 4, Eq. 11). Co-dependence of (**b**) α_E and α_{NADPH} and (**c**) λ and α_{TH}, across all variable space of the initial conditions of Scenario 2, calculated for R_{BP} from the isotope flux balance of biphytane synthesis (Figure 4; Eq. 13). Individual data points are Monte Carlo simulation results. Orange curve in (**b**): $y = 0.669/x$. Boundaries (dashed lines) in (**c**) mark the suggested minimum and maximum values of α_{TH} (0.222, PntAB; 0.566 sTH; Wijker et al., 2019). The observed range suggests λ is no greater than ~0.06 (6% inefficiency of NADH hydride transfer; main text Figure 4).

Supplemental References:

Friedrich, P., Darley, D.J., Golding, B.T., and Buckel, W. (2008) The Complete Stereochemistry of the Enzymatic Dehydration of 4-Hydroxybutyryl Coenzyme A to Crotonyl Coenzyme A. *Angew Chem Int Ed* **47**: 3254–3257.

Leavitt, W.D., Flynn, T.M., Suess, M.K., and Bradley, A.S. (2016) Transhydrogenase and Growth Substrate Influence Lipid Hydrogen Isotope Ratios in Desulfovibrio alaskensis G20. *Front Microbiol* **07**:

WÖLFLE, K., MICHENFELDER, M., KÖNIG, A., HULL, W.E., and RÉTEY, J. (1986) On the mechanism of action of methylmalonyl-CoA mutase: Change of the steric course on isotope substitution. *Eur J Biochem* **156**: 545–554.

Supplemental Tables 1 & 2

Supplemental Table S1: Hydrogen Sources.

Full accounting of H sources to the biphytanes of archaeal tetraethers for organisms producing acetyl-CoA autotrophically via the 3HP/4HB pathway (assuming water H:NADPH = 2:1, i.e., 0.6667:0.3333. See also main text Figure 3, and main text Tables 2, 3. Raw data and processing scripts for GC-P-IRMS output are available at: https://github.com/KopfLab/2022_leavitt_et_al.

			Number of H in Biphytane				Fractions - detailed				Fractions-simplified			
							f_{GGR_W} / $f_{LipSynth\_W}$	$f_{GGR\_NAD(P)H}$ / $f_{LipSynth\_NADPH}$	f_{GGR_Fd} / n/a	n/a / f_x	f_{*W}	f_{*NADPH}	f_{Fd}	f_x
			H_2O	NADPH	Fd	H2O_Exch	H_2O	NADPH	Fd	H2O_Exch	H_2O	NADPH	Fd	H2O_Exch
Scenario 1	BP0	GGR	8	8	0	--	0.1000	0.1000	0	--	0.5028	0.4972	0	0
		LipSynth	32.222	31.778	--	0	0.4028	0.3972	--	0				
	BP1	GGR	7.333	7	0	--	0.0940	0.0897	0	--	0.5071	0.4929	0	0
		LipSynth	32.222	31.444	--	0	0.4131	0.4031	--	0				
	BP2	GGR	6.667	6	0	--	0.0877	0.0789	0	--	0.5117	0.4883	0	0
		LipSynth	32.222	31.111	--	0	0.4240	0.4094	--	0				
	BP3	GGR	6.000	5	0	--	0.0811	0.0676	0	--	0.5165	0.4835	0	0
		LipSynth	32.222	30.778	--	0	0.4354	0.4159	--	0				
Scenario 2	BP0	GGR	8	0	8	--	0.1000	0	0.1000	--	0.5028	0.3972	0.1000	0
		LipSynth	32.222	31.778	--	0	0.4028	0.3972	--	0				
	BP1	GGR	7.333	0	7	--	0.0940	0	0.0897	--	0.5071	0.4031	0.0897	0
		LipSynth	32.222	31.444	--	0	0.4131	0.4031	--	0				
	BP2	GGR	6.667	0	6	--	0.0877	0	0.0789	--	0.5117	0.4094	0.0789	0
		LipSynth	32.222	31.111	--	0	0.4240	0.4094	--	0				
	BP3	GGR	6.000	0	5	--	0.0811	0	0.0676	--	0.5165	0.4159	0.0676	0
		LipSynth	32.222	30.778	--	0	0.4354	0.4159	--	0				
Scenario 3	BP0	GGR	8	8	0		0.1000	0.1000	0		0.3000	0.4000	0	0.3000
		LipSynth	16	24	--	24	0.2000	0.3000	--	0.3000				
	BP1	GGR	7.333	7	0		0.0940	0.0897	0		0.2991	0.3932	0	0.3077
		LipSynth	16	23.667	--	24	0.2051	0.3034	--	0.3077				
	BP2	GGR	6.667	6	0		0.0877	0.0789	0		0.2982	0.3860	0	0.3158
		LipSynth	16	23.333	--	24	0.2105	0.3070	--	0.3158				
	BP3	GGR	6.000	5	0		0.0811	0.0676	0		0.2973	0.3784	0	0.3243
		LipSynth	16	23.000	--	24	0.2162	0.3108	--	0.3243				
Scenario 4	BP0	GGR	8	0	8		0.1000	0	0.1000		0.3000	0.3000	0.1000	0.3000
		LipSynth	16	24	--	24	0.2000	0.3000	--	0.3000				
	BP1	GGR	7.333	0	7		0.0940	0	0.0897		0.2991	0.3034	0.0897	0.3077
		LipSynth	16	23.667	--	24	0.2051	0.3034	--	0.3077				
	BP2	GGR	6.667	0	6		0.0877	0	0.0789		0.2982	0.3070	0.0789	0.3158
		LipSynth	16	23.333	--	24	0.2105	0.3070	--	0.3158				
	BP3	GGR	6.000	0	5		0.0811	0	0.0676		0.2973	0.3108	0.0676	0.3243
		LipSynth	16	23.000	--	24	0.2162	0.3108	--	0.3243				

Supplemental Table S2: NADP(H) Source Mechanisms in *N. maritimus.* BLAST approach employed as by (Leavitt et al., 2016).

Enzyme name	NAD(P)H generating	Abbreviation	H-isotope category	Pathway	Nitrosopumilus maritimus SCM1 locus tag(s)
Complex 1: NADH:ubiquinone oxidoreductase	Yes	Nuo	2b	N/A	N_mar_0276 to 0286
Ferredoxins	Yes	Fd	2b, 3	N/A	N_mar_0238, 0239, 1537, 1765
ferredoxin:NADP+ oxidoreductase	Yes	FNR	*3*	N/A	Nmar_0672
cytosolic NADP+-reducing hydrogenase	Yes	SH	3 or 2	N/A	Nmar_1389
cytosolic NADP+-reducing hydrogenase	Yes	SH	3 or 2	N/A	Nmar_0267
cytosolic NADP+-reducing hydrogenase	Yes	SH	3 or 2	N/A	Nmar_0253
NAD+ kinase	Yes	NADK	2	N/A	Nmar_0268, Nmar_0440, Nmar_0921
isocitrate dehydrogenase	Yes	IDH	2	TCA cycle	Nmar_1069, Nmar_1379
glucose-6-phosphate dehydrogenase	Yes	G6PDH	2	oxPPP, ED	Nmar_0168
6-phosphogluconate dehydrogenase	Yes	6PGDH	2	oxPPP	Nmar_0635
glucose dehydrogenase	Yes	GDHs	2	Modified EDs	Nmar_0369
non-phosphorylating glyceraldehyde 3-phosphate dehydrogenase	Yes	GAPN	2	EMP, ED, SP ED	Nmar_1608
NAD+-dependent glyceraldehyde phosphate dehydrogenase, phosphorylating	Yes	NAD+/GAPDH	2	EMP, ED, SP ED	Nmar_0831
D-glyceraldehyde dehydrogenase (NADP+)	Yes	NADP+/GADH	2	npED	Nmar_1608
2-ketoglutarate (oxoacid)/ ferredoxin oxidoreductase			2	TCA cycle	Nmar_0413, Nmar_0414
malate dehydrogenase	Yes		2	TCA cycle	Nmar_0338, Nmar_0676

/END